Journal of Sound and Vibration 513 (2021) 116413

Contents lists available at ScienceDirect

Journal of Sound and Vibration

journal homepage: www.elsevier.com/locate/jsvi

Dynamics of pulse-loaded circular Föppl-von Kármán thin plates-Analytical and numerical studies

N. Mehreganian [a], M. Toolabi [b], Y.A. Zhuk [c], F. Etminan Moghadam [c], L.A. Louca [a], A. S. Fallah [d,*]

[a] Department of Civil & Environmental Engineering, Skempton Building, South Kensington Campus, Imperial College London, London SW7 2AZ, UK
[b] Department of Mechanical Engineering, City and Guilds Building, South Kensington Campus, Imperial College London, London SW7 2AZ, UK
[c] Department of Theoretical and Applied Mechanics, Faculty of Mechanics and Mathematics, Taras Shevchenko National University of Kyiv, Glushkova Ave. 4E, Kyiv 03022, Ukraine
[d] Department of Mechanical, Electronic, and Chemical Engineering, OsloMet, Pilestredet 35, St. Olavs plass, Oslo NO-0130, Norway

ARTICLE INFO

Keywords:
FVK plate
pulse loading
PL perturbation method
Frobenius method
FSI
closed-form solution

ABSTRACT

Materials such as modern armour steel, benefit from appreciably high elastic energy storage capacity prior to failure. Such a capacity contributes to absorption of the impulse generated during an extreme pulse pressure loading event such as a localised blast. As the plate deforms within the bounds of the elastic region without plastic dissipation, the probability of catastrophic failure is mitigated while large deformations compared to conventional metallic panels are encountered. No studies have proposed, to date, a closed-form solution for nonlinear elastic response of thin circular plates subject to localised pulse loads.

The present work aims at deducing, from the minimization of the Föppl-von Kármán (FVK) energy functional, explicit solutions for the response of dynamically (pulse) loaded thin clamped circular plates undergoing large deformations. The solutions were derived from a presumed kinematically admissible displacement field together with an associated stress tensor potential as an infinite polynomial series, which was truncated into a multiplicative decomposition of temporal parts and spatial parts, representative of a Multiple Degrees-of-Freedom (MDOF's) system.

In the case of static loading, using the Frobenius method, an exact recursive solution to each mode of defamation was obtained. In the event of dynamic loading, useful expressions for stress tensor components were delineated, corresponding to a multimode multiplicative product, and a series of coupled Ordinary Differential Equations (ODE's) were derived, using the Ritz-Galerkin variational method. The explicit solutions were sought using the Poincaré-Lindstedt (PL) perturbation method. The closed-form solutions obtained were corroborated with FE results including the Fluid-Structure Interaction (FSI) effects and showed convergence when the first few modes were considered. The influence of higher modes, however, on the peak deformation was negligible and the solution with 3 DOF's conveniently estimated the blast response to a satisfactory level of precision. The influence of element type on the response was also examined and discussed in the context of the problem.

* Corresponding author.
E-mail address: arashsol@oslomet.no (A.S. Fallah).

https://doi.org/10.1016/j.jsv.2021.116413
Received 28 February 2021; Received in revised form 9 August 2021; Accepted 18 August 2021
Available online 19 August 2021

Notations

A_{1-n}	Frobenius coefficients/displacement modes [Various]
C_{1-n}	Stress potential parameters [Various]
D_1	Flexural rigidity $[ML^2T^{-2}]$
E	Young's modulus $[ML^{-1}T^{-2}]$
$E_1 - E_4$	Integration constant [Various]
$F_1 - F_4$	Integration constants [Various]
G_i	Membrane Stiffness function of an MDOF system $[ML^4T^{-2}]$
I_p	Transmitted impulse $[MLT^{-1}]$
K	Membrane stiffness coefficient (SDOF system) $[L^6T^{-2}]$
L_e	Charge width $[L]$
M_e	Charge mass $[M]$
N_r	Radial membrane force $[MLT^{-2}]$
N_θ	Circumferential membrane force $[MLT^{-2}]$
Q_r	Shear force $[MLT^{-2}]$
R	Plate radius $[L]$
$\overline{W}$	Dimensionless Mid-Point transverse displacement [1]
P_0	Transmitted overpressure $[ML^{-1}T^{-2}]$
Z	Scaled distance $[LM^{-1/3}]$
$\widehat{a}_0, a_s$	Speed of sound $[LT^{-1}]$
c_k	Amplitude of vibration of $k/2$ $^{\text{th}}$ mode [Various]
h	Plate thickness $[L]$
l	Slenderness parameter [1]
$p_2(t)$	Temporal part of pulse pressure [1]
$p^*(r,t)$	Pressure function $[ML^{-1}T^{-2}]$
p_s	Overpressure $[ML^{-1}T^{-2}]$
q_1, q_2	Frobenius exponents [1]
r	Generalised radius of the polar coordinate $[L]$
t_0^*	Characteristic time of the FSI $[T]$
t_d	Duration of the load; $[T]$
u_r	Radial displacement $[L]$
u_θ	Circumferential displacement [1]
w	Transverse displacement $[L]$
$\overline{W}^{(i)}$	Normalised transverse displacement of i$^{\text{th}}$ iteration [1]
$\mathscr{S}(a,b)$	FVK Operator [Various]
$\mathscr{L}(\mathrm{a},\mathrm{b})$	Differential operator [Various]
β_0	Impulse reduction factor [1]
β_{1-3}	Integration constant parameters [1]
ε_0	Perturbation parameter [1]
$\varepsilon_{\theta\theta}$	Circumferential strain [1]
ε_{rr}	Radial strain [1]
$\varepsilon_{r\theta}$	Shear strains [1]
$\mathbf{\Phi}(r,t)$	Stress potential function $[MLT^{-2}]$
$\widehat{\phi_{\mathrm{k}}}(\mathrm{t})$	Temporal part of the Stress potential function [Various]
$\overline{\phi}^{(\mathrm{i})}$	Dimensionless static Stress potential function [1]
μ	Areal density $(=\rho h)$; $[ML^{-2}]$
ν	Poisson's ratio; [1]
σ_{rr}	Radial stress tensor $[ML^{-1}T^{-2}]$
$\sigma_{\theta\theta}$	Circumferential stress tensor $[ML^{-1}T^{-2}]$
ρ	Plate density $[ML^{-3}]$
ρ	Undisturbed density of air $[ML^{-3}]$
$\tau\tau$	Normalised vibration time; [1]
τ_d	Normalised duration of the pulse; [1]
θ	Generalized rotation of the polar coordinate [1]
$\overline{\omega}_1$	First vibration pseudo frequency $[T^{-1}]$
$\overline{\omega}_2$	Second vibration pseudo frequency; $[T^{-1}]$
$\omega_{0\mathrm{k}}$	Modal vibration frequency $[T^{-1}]$

1. Introduction

Extensive pulse pressure loads generated by a high explosive detonation or a gas explosion (deflagration) are calamitous and detrimental to property and life, with potentially disastrous effects to structures as well as high human toll. Events such as the recent Beirut explosion (2020), Buncefield incident (2005), London bombing (2005), and Piper Alpha (1988) signify the importance of safe structural design against extensive shock and blast loads. One vein to mitigate the impact of such pressure loads is by the choice of high strength armour steel materials. This class of steel allows for large elastic deformations and energy dissipation in subsequent vibration in contradistinction to mild steel which allows for energy dissipation mechanisms through plastic deformation.

The actual physics of the blast phenomenon is complex and to gain an understanding based on computational models entails the implementation of Fluid-Structure Interaction (FSI) as well as Computational Fluid Dynamics (CFD) algorithms on the top of those related to elastic, plastic, and fracture solid mechanics. The extensive load potentially leads to large deformation of the plate. In such circumstances, the evolved membrane (catenary) forces, brought about by finite displacements, find out-of-plane projections which help to resist the out-of-plane deformations, at the cost of a surge in the in-plane tensile stresses.

Concerning free air blast effects on high strength materials, Zakrisson [1] performed experimental and numerical studies of close-in free air and ground blasts on WELDOX 700E steel plates, generated by cylindrical NSP71 plastic explosive (PE4) of 20.66mm height and the diameter-to-height ratio of 3. The numerical methods entailed 2D and 3D FSI techniques. Following a convergence study, the element size of the Eulerian domain was adjusted to 4mm for a target plate of 600mm length. Zakrisson [2] and Tyas et al [3, 4] investigated the soil-plate interaction deformation from buried explosives. In the case of buried explosives, the momentum transfer due to the combined pulse pressure and mass impact of soil grains generates more detrimental combined effects of momentum transfer from sand impact and the energetics output. The latter authors examined the temporal and spatial distributions of close-in blasts [5]. Comparing various numerical techniques, Børvik et al. [6] observed a significant difference in the transient deformation of the box containers subject to confined (internal) blast pressure, despite the same impulse as the free air counterpart. Aune et al. [7, 8] monitored and reported on the transient deformation of steel plates subjected to far-field pulse pressures examined experimentally.

Rigby et al [9] examined the negative phase of the scenario considering small-scaled distances. The negative phase of the impulse and peak underpressure is negligible relative to the positive phase and overpressure. Wierschem et al. [10] examined the attenuation of blast waves on a base structure of 5.13m height consisting of 9 floors and equipped with six nonlinear vibration absorbers. They showed that when the vibration absorbers are unconstrained (free to move relative to the structure floor) a rapid decay in the vibration amplitude occurs due to the frequency scattering of the blast energy.

In practical applications of extensive blast loads whereupon the response exceeds the bounds set for the elastic region, finding the plastic deformations is difficult since these are interspersed with the elastic deformations [11]. However, a considerable body of literature exists on the dynamic plastic response of plates and shells (beams as a special case) subjected to impact and blast loading, based on the limit analysis methods built up over the past decades [12–18]. Such methods assume the material behaviour as rigid-perfectly plastic or elastic-perfectly plastic with associated constitutive equations characterising individually, or in combination, the effects of bending moments, membrane and/or transverse shear forces. Under moderate pulse pressure loads, a considerable portion of the transferred energy into the structure made of these materials is stored as elastic energy and expended through heat in residue vibration rather than being dissipated plastically. Under such circumstances, the load-bearing capacity of the structure in the elastic zone shall not be ignored.

The Föppl-von Kármán (FVK) expressions form a powerful tool to capture the pronounced transverse deformations of thin elastic plates and the corresponding membrane stresses, using minimal geometric nonlinearity. While the analyses of plates and shells using the FVK strains to address the blast resistance of plates have been extensively used in the literature [19-24], the use of FVK expressions spans to aerospace engineering [25], instability of the composites and isotropic plates to thermal loads [26-30], and bistability of morphing structures [31].

Early works to dispose of the FVK expressions to arrive at manageable solutions for a variety of geometrically nonlinear problems relied on the discrete approximation techniques as carried out by Mansfield [32] and later extended by researchers [28, 29]. This procedure assumes a uniform curvature field with sufficiently low degrees of freedom to reduce the FVK functional to a finite-dimensional subspace, hence deriving the solutions to membrane stresses.

For high dimensional nonlinear systems, there exist different forms of nonlinear vibrations due to the existence of modal interactions. In the case of damped vibrations, internal resonant relationships between the modal linear frequencies may lead to large deformations [33]. Asymptotic perturbation techniques have also been extensively used in the studies of nonlinear vibrations [33-38], using Föppl Von Kármán nonlinear kinematics and Reddy's third-order shear deformation theory. Teng et al [39] developed a theoretical solution for the transient vibrations of simply supported and clamped FVK rectangular plates, based on the first modes of Fourier half expansion series to describe the spatial component of the transverse displacement field. Lighthill's extension of Poincaré's perturbation technique was utilised to delineate estimates for the Airy stress function at each time step.

Early works of Taylor [40] revealed that the impulse imparted to flexible structures is reduced by the Fluid-Structure Interaction effects, primarily in thin plates, due to the acquisition of the instantaneous velocity, thus relieving the plate off the applied pressure. This work was extended by Kambouchev et al [41, 42] to account for fluid compressibility. The transmitted impulse was derived based on acoustics to intense shock wave limits for light and intermediate plate weights. Assuming an exponential decay type for the incident wave overpressure p_s, the pressure transmitted to the plate is expressed as:

$$P_0 = \frac{2p_s}{\beta_0 - 1}\left[\beta_0 e^{-\frac{\beta_0 t}{t_d}} - e^{-\frac{t}{t_d}}\right], \tag{1}$$

where the dimensionless factor $\beta_0 = \rho_0 \widehat{a}_0 t_d / \rho h$ may be visualised as the relative inertia of the volume of the compressed gas and the plate, equivalent to the relative duration of the incident wave and that of the interaction (t_d/t_0^*), with ρ_0 being the undisturbed gas density, $\widehat{a}_0$ the speed of sound in the gaseous medium, while $t_0^* = \mu/(\rho_0\ \widehat{a}_0)$ is interpreted as the characteristic time of the FSI [41, 42]. The impulse transmitted to the plate was derived as $I_p = 2p_s t_d \beta_0^{\frac{\beta_0}{1-\beta_0}}$. In the case of light plates, the limit ratio of the transmitted impulse to the incident impulse degenerates to $2/\beta_0$.

Although the mass and stiffness of the plate have most of the influence on the transmitted impulse, boundary conditions also play a significant role in the portion of the total impulse imparted to the plate. Pressure recirculation occurs by the boundaries of monolithic rectangular plates subjected to localised blasts generated from a PE4 of charge diameter a third of the plate width and stand-off distance 13mm, hence the total transmitted impulse can be reduced by up to 35% [43].

In the experimental observations of Tyas et al [5], the close-in blast overpressure recorded with Hopkinson pressure bar did not comprise a transient decay as modelled by Friedlander equation but rather showed a more complex behaviour. As the impact-induced stress wave propagated along a cylindrical bar, each Fourier frequency component travelled with a different velocity, which gave rise to the well-known Pochammer-Chree dispersion.

The present work employs the well-established Föppl Von Kármán model to examine the influence of finite displacements on the transient dynamic response of thin circular plates, in the light of the multi-mode coupling of bending and membrane stresses.

This paper is organised into 6 sections. Following this introduction, the governing equations of motion are derived for the thin circular plate in Section 2 based on the nonlinear elastic model. Then the exact theoretical solution of such plates subject to static loading conditions are sought and the results are presented in Section 3. In Section 4 the analysis is extended to dynamic loads in two distinct phases of motion, namely forced- and free-vibrations. The theoretical solutions are then validated against the Finite Element (FE) models in Section 5, using the advanced Multi-Material Arbitrary Lagrangian-Eulerian (MMALE) technique. The objective of this technique is to investigate the validity of the models against the actual pulse pressures involving FSI phenomena. Finally, in Section 6 the conclusions of this study are presented and discussed.

2. Governing equations

2.1. Pressure load

Consider a monolithic circular plate of radius R and thickness h, which is made of isotropic material. The plate is initially flat and subjected to a transverse pulse pressure load, which is assumed to remain orthogonal to the plane of plate orientation during the loading. The loading is characterised as a single term of the multiplicative decomposition of its spatial (load shape) and temporal (pulse shape) parts, viz. $p^*(r,t) = p_1(r)p_2(t)$, the former (spatial part) is assumed to maintain uniform pressure across the characteristic area of the plate, i.e. $p_1(r) = P_0$. While various functions may be prescribed for the latter (temporal part) of the loading, i.e. exponential, sinusoidal, linear, or rectangular [44-46], in this work, the latter has been assumed in the dynamic analyses here, which may be representative of an impulsive loading case. Thus, the piecewise function characterising the temporal part becomes $p_2(t) = 1$ for a duration of the interval $0 \le t \le t_d$ and $p_2(t) = 0$ beyond this interval. By further simplification, the negative phase of the pressure is disregarded and excluded from the analyses, which limits the work to the pulse pressures generated from moderate scaled distance sources. The influence of the negative phase may be examined by introducing a successive phase of motion using the prescribed functions of the load [8, 9] and applying the associated kinematic conditions to the derived solutions at such phase, which falls beyond the scope of this study.

The general expressions for the strain tensor in terms of the displacement field $u(r,\theta)$ (with component $u_r(r,\theta)$ and $u_\theta(r,\theta)$) in Polar Coordinates are expressible as:

$$\varepsilon_{rr} = \frac{\partial u_r}{\partial r} + \frac{1}{2}\left[\left(\frac{\partial u_r}{\partial r}\right)^2 + \left(\frac{\partial u_\theta}{\partial r}\right)^2\right], \tag{2}$$

$$\varepsilon_{\theta\theta} = \frac{1}{r}\left(\frac{\partial u_\theta}{\partial \theta} + u_r\right) + \frac{1}{2r^2}\left[\left(\frac{\partial u_r}{\partial \theta} - u_\theta\right)^2 + \left(\frac{\partial u_\theta}{\partial \theta} + u_r\right)^2\right], \text{ and} \tag{3}$$

$$\varepsilon_{r\theta} = \frac{1}{r}\left(\frac{\partial u_r}{\partial \theta} - u_\theta + r\frac{\partial u_\theta}{\partial r}\right) + \frac{1}{2}\left[\frac{1}{r}\frac{\partial u_r}{\partial r}\left(\frac{\partial u}{\partial \theta} - u_\theta\right) + \frac{1}{r}\frac{\partial u_\theta}{\partial r}\left(\frac{\partial u_\theta}{\partial \theta} + u_r\right)\right]. \tag{4}$$

The second-order terms in Eqs. (2)-(4) represent the membrane strains whose associated deformation gradients are the sole contributors to geometric nonlinearity. The compatibility condition of strains is given by:

$$r\frac{\partial^2 \gamma_{r\theta}}{\partial r \partial \theta} + \frac{\partial \gamma_{r\theta}}{\partial \theta} = \frac{\partial^2 \varepsilon_{rr}}{\partial \theta^2} + r^2\frac{\partial^2 \varepsilon_{\theta\theta}}{\partial r^2} - r\frac{\partial \varepsilon_{rr}}{\partial r} + 2r\frac{\partial \varepsilon_{\theta\theta}}{\partial r}. \tag{5}$$

Now, using the transformation from Cartesian to Polar Coordinates, the FVK Equations giving the fundamental description of nonlinear elastic dynamics of the thin plate read [47] as follows:

$$\frac{D_1}{h}\nabla^2\nabla^2 w = \mathscr{S}(w,\boldsymbol{\phi}) + \frac{p^*(r,t) - \mu\dot{w}}{h}, \text{ and} \tag{6}$$

$$\frac{1}{E}\nabla^2\nabla^2\boldsymbol{\phi} = -\frac{1}{2}\mathscr{S}(w,w), \tag{7}$$

where $\nabla^2(\psi)$ and $\mathscr{S}(\boldsymbol{w},\Phi)$ represent the Laplacian and differential operators, which are expressible, respectively, by Eqs. (8) and (9) as:

$$\nabla^2(w) = \frac{\partial^2(w)}{\partial r^2} + \frac{1}{r}\frac{\partial(w)}{\partial r} + \frac{1}{r^2}\frac{\partial^2(w)}{\partial\theta^2}, \tag{8}$$

$$\mathscr{S}(w,\boldsymbol{\Phi}) = \frac{\partial^2 w}{\partial r^2}\left(\frac{1}{r}\frac{\partial\boldsymbol{\Phi}}{\partial\theta} + \frac{1}{r^2}\frac{\partial^2\boldsymbol{\Phi}}{\partial\theta^2}\right) + \frac{\partial^2\boldsymbol{\Phi}}{\partial r^2}\left(\frac{1}{r}\frac{\partial w}{\partial r} + \frac{1}{r^2}\frac{\partial^2 w}{\partial\theta^2}\right) - 2\frac{\partial}{\partial r}\left(\frac{1}{r}\frac{\partial\boldsymbol{\Phi}}{\partial\theta}\right)\frac{\partial}{\partial r}\left(\frac{1}{r}\frac{\partial w}{\partial r}\right). \tag{9}$$

Eq. (7) is essentially a compatibility equation, where $\Phi(r,t)$ represents the stress potential (Airy stress function), with $D_1 = \frac{Eh^3}{12(1-\nu^2)}$ representing the plate flexural rigidity. As is customary, the overdot represents differentiation with respect to time. The generalised coordinates are measured from the centre of the plate in the reference configuration. As the loading is axisymmetric, the deformation of the plate is independent of the polar coordinate θ. Thus, with some algebraic manipulations, the FVK expressions boil down to the following coupled system of Partial Differential Equations (PDE's):

$$\left(\frac{dw}{dr}\right)^2 = -\frac{2}{E}\left(\frac{d}{dr}\left(\frac{rd^2\Phi}{dr^2}\right) - \frac{1}{r}\frac{d\Phi}{dr}\right), \text{ and} \tag{10}$$

$$\frac{dw}{dr}\frac{d\Phi}{dr} + \int\frac{1}{h}(P_0 r - \mu r..w^{\cdot\cdot})dr = \frac{D_1}{h}\left(\frac{d}{dr}\left(\frac{rd^2 w}{dr^2}\right) - \frac{1}{r}\frac{dw}{dr}\right). \tag{11}$$

The following non-dimensional parameters are introduced to generalise the study:

$$\overline{w} = \frac{w}{h},\ \overline{\phi} = \boldsymbol{\phi}\Big/Eh^2,\ p = P_0\Big/E,\ \overline{r} = r\Big/R,\ \text{and } l = \frac{R}{h}. \tag{12a-e}$$

Utilising Eqs. (12a-e) and substituting them into Eqs. (10)-(11), the FVK expressions are recast in the dimensionless form as:

$$\left(\frac{d\overline{w}}{d\overline{r}}\right)^2 = -2\mathscr{L}\left(\overline{\phi},\overline{r}\right), \tag{13}$$

$$\frac{d\overline{w}}{d\overline{r}}\frac{d\overline{\phi}}{d\overline{r}} + \int\left(p - \frac{h^2}{a_s^2}..w^{\cdot\cdot}\right)l^4\overline{r}d\overline{r} = \frac{1}{12(1-\nu^2)}\mathscr{L}(\overline{w},\overline{r}), \text{ with} \tag{14}$$

$$\mathscr{L}(\overline{w},\overline{r}) = \frac{d}{d\overline{r}}\left(\frac{\overline{r}d^2(\overline{w})}{d\overline{r}^2}\right) - \frac{1}{\overline{r}}\frac{d(\overline{w})}{d\overline{r}}, \tag{15}$$

where $a_s = \sqrt{E/\rho}$ is the speed of the sound wave propagating through the solid medium.

3. Static Loading

Since the FVK expressions of Eqs. (10) and (11) work in tandem, the undertaken approach herein resorts to an iterative procedure to simplify the Partial Differential Equation (PDE) form of the FVK expressions to a set of reduced, second-order Ordinary Differential Equations (ODE). However, in the case of static loading, where the inertia term from Eq. (14) vanishes; an exact solution to the displacement field of the plate may be sought using the mathematical approach outlined as follows:

1 Assume an ansatz for Airy stress function.
2 Evaluate the displacement field from Eq. (14).
3 Update the expression of stress potential function using Eq. (13).
4 Repeat the procedure from step 2 to step 4.

The nonlinear displacement field is obtained through this iterative procedure, while expressed as a truncated infinite sum of its modes with a recursive expression. Applying the iterative procedure, the interdependence of Eqs. (10) from (11) (or vice versa) may be recast into:

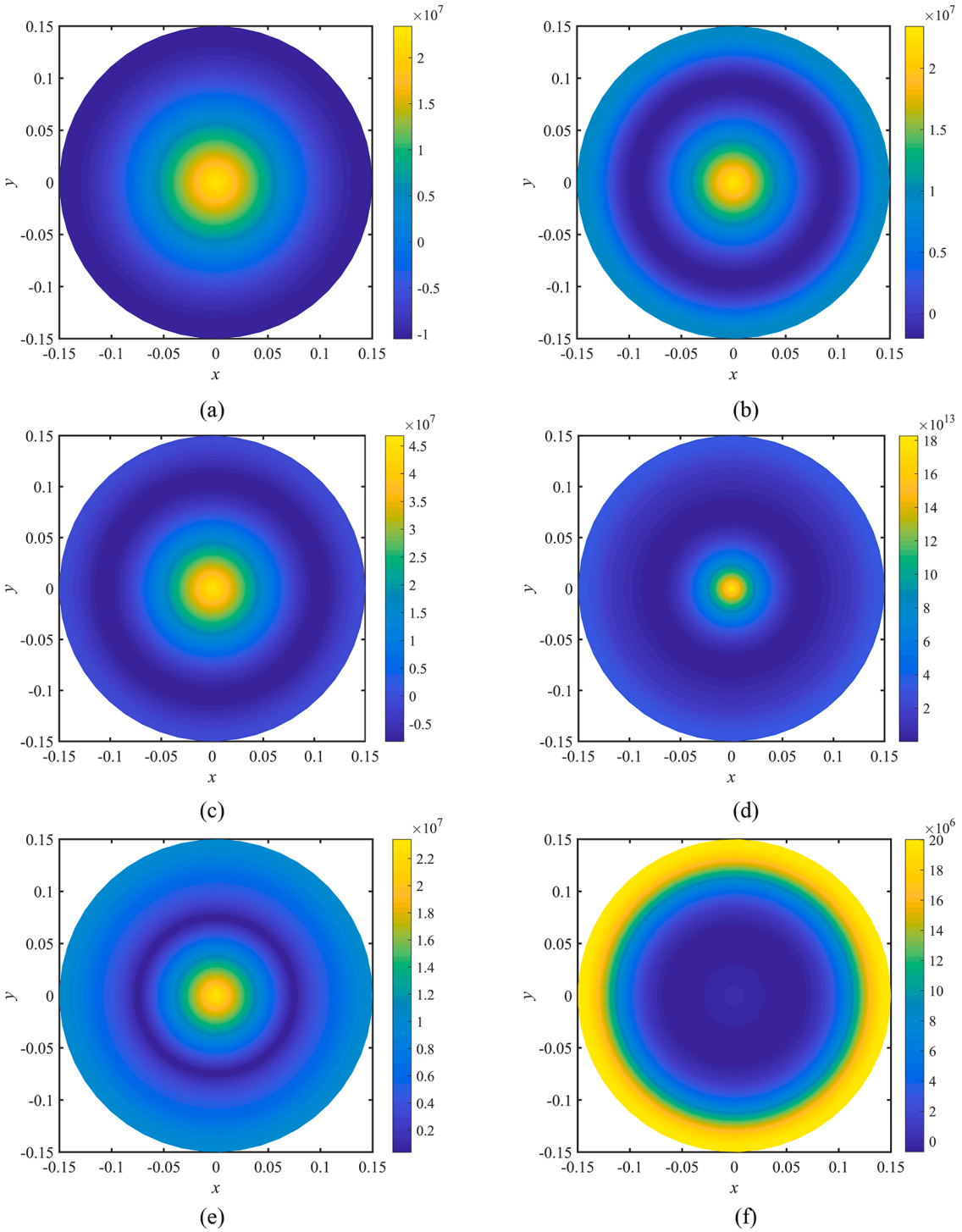

Fig. 1. Variation of the principal stresses, (a) radial and (b) circumferential stresses in the plate, the contour plot of the first stress invariants $I_1 = \sigma_{rr} + \sigma_{\theta\theta}$ and the second $J_2 = \frac{1}{2}s_{ij}s_{ij}$, where $s_{ij} = \sigma_{ij} - \frac{1}{3}\sigma_{kk}\delta_{ij}$ represents the deviatoric stress tensor, are shown in (c) and (d), respectively. Figures (e) and (f) represent the von Mises $\sigma_e = \sqrt{3J_2}$ and Tresca $\sigma_T = \sigma_{\theta\theta} - \sigma_{rr}$ stress tensors, respectively. The units of the abscissa and ordinate axes are in [m] while the stress values are given in [Pa].

$$\left(\frac{d\overline{w}^{(i+1)}}{d\overline{r}}\right)^2 = -2\mathscr{L}\left(\overline{\phi}^{(i)}, \overline{r}\right), \text{ and} \tag{16}$$

$$\frac{d\overline{w}^{(i+1)}}{d\overline{r}}\frac{d\overline{\phi}^{(i)}}{d\overline{r}} + \frac{p\overline{r}^2}{2} = \frac{1}{12(1-\nu^2)}\mathscr{L}\left(\overline{w}^{(i+1)}, \overline{r}\right), \tag{17}$$

where the superscript indices (i = 0, 1, 2, …) denote the iteration steps: The Dirichlet Boundary Conditions and force equilibrium expressions for the clamped plate along its periphery dictate that [47, 48]:

$$\overline{w}(1) = \overline{w}'(1) = 0,\ Q_r(0) = 0,\ \psi'(1) = \frac{1+\nu}{2}\psi(1),\ r\frac{dN_r}{dr} + N_r - N_\theta = 0, \text{ and} \tag{18a-d}$$

$$r\frac{dN_r}{dr}|_R + (1-\nu)N_r(r=R) = 0, \tag{19}$$

where $\psi(\overline{r}) = Eh^2\overline{r}\frac{d\overline{\phi}}{d\overline{r}}$, and N_r and N_θ represent the radial and circumferential components of the membrane force, respectively. The radial and circumferential stresses are thus determined as

$$\sigma_{rr} = El^{-2}\frac{1}{\overline{r}}\frac{d\overline{\phi}}{d\overline{r}}, \sigma_{\theta\theta} = El^{-2}\frac{d^2\overline{\phi}}{d\overline{r}^2}, \tag{20a-b}$$

and the shear force Q_r at the centre is given as:

$$Q_r = -\frac{d}{dr}\nabla^2(w(r)). \tag{21}$$

The first iterative value of the transverse displacement is unequivocally sought by setting $\overline{\phi}^{(0)} = 0$ in Eq. (17) and solving the ODE, given as:

$$\overline{w}^{(1)} = \frac{3}{16}pl^4\left(1-\nu^2\right)\left(1-\overline{r}^2\right)^2. \tag{22}$$

Substituting this expression in Eq. (16) and solving the ODE yields the first non-zero estimate of $\overline{\phi}$ as:

$$\overline{\phi}^{(1)} = C_1 + \frac{C_2\overline{r}^2}{2} + C_3 ln(\overline{r}) + \beta_1\overline{r}^8 + \beta_2\overline{r}^6 + \beta_3\overline{r}^4, \tag{23}$$

from which we immediately obtain $C_3 = 0$, as the stresses remain finite at the plate centre. Note that there are no odd powers of the spatial variable $\overline{r}$ in the expression of the stress potential function, whose form turns out to be conducive to reduce the derived terms of the displacement field. The coefficient C_2 may be determined from either BC's in Eq. (18c) or (19) as:

$$C_2 = \frac{16(6\beta_1 + 3\beta_2 + \beta_3)}{R(1+\nu) - 4} - 2(4\beta_1 + 3\beta_2 + 2\beta_3). \tag{24}$$

where the coefficients $\beta_1 - \beta_3$ are expressed in (A. 1 a-c). The variations of the radial and circumferential stresses based on the above stress potential function are illustrated in Fig. 1. Substituting Eqs. (23)-(24) back into Eq. (16) gives:

$$Rf_1(\overline{r})\frac{d\overline{w}}{d\overline{r}} + \overline{r}\frac{d^3\overline{w}}{d\overline{r}^3} + \frac{d^2\overline{w}}{d\overline{r}^2} - 6l^4p\overline{r}^2\left(1-\nu^2\right) = 0, \tag{25}$$

where $f_1(\overline{r}) = \frac{1}{\overline{r}R}\left(f(\overline{r}) - \frac{1}{4}\right)$ depends on $f(\overline{r})$ as defined in the sequel by Eq. (27). Using the transformation $\hat{u}(\overline{r}) = l^{-1}\sqrt{\overline{r}R}d\overline{w}/d\overline{r}$, derived from Polyanin's method for ODE's [49], a reduced form of Eq. (25) is attained. The resulting ODE is furnished into:

$$f(\overline{r})\hat{u}(\overline{r}) + \overline{r}^2\frac{d^2\hat{u}(\overline{r})}{d\overline{r}^2} = \frac{P_0R^2}{2D_1}\overline{r}^2, \tag{26}$$

where $f(\overline{r})$ is a polynomial function of degree 8 derived as:

$$f(\overline{r}) = -\frac{3}{4} + a_0R^2\overline{r}^2 + b_0R^4\left(\overline{r}^4 - \frac{2}{3}\overline{r}^6 + \frac{1}{6}\overline{r}^8\right), \tag{27}$$

where the coefficients a_0 and b_0 are expressed in (A. 3a-b). The ODE in Eq.(26) is not analytic at $\overline{r} = 0$ due to singularity, a requisite condition to seek the solution by using the Frobenius method [36, 50]. Toward this end, the rotational function $u(\overline{r})$ is assumed as a hypergeometric series:

$$\widehat{u}(\bar{r}) = \sum_{k=0}^{\infty} A_k (\bar{r}R)^{k+q}. \tag{28}$$

Substituting Eq. (27)-(28) in (26) and using truncation yields:

$$\sum_{k=0}^{\infty} a_0 A_k (\bar{r}R)^{k+q+2} + b_0 A_k (\bar{r}R)^{k+q+4} + -\frac{2}{3} b_0 R^{-2} A_k (\bar{r}R)^{k+q+6} + \frac{1}{6} b_0 R^{-4} A_k (\bar{r}R)^{k+q+8} + \sum_{k=0}^{\infty} \left(-\frac{3}{4} + (k+q)(k+q-1) \right) A_k (\bar{r}R)^{k+q} = \frac{P_0 R^{\frac{7}{2}} \bar{r}^{\frac{7}{2}}}{2D_1}, \tag{29}$$

The indicial polynomial is recovered by satisfying the expression at the plate centre and using the conditions $f(0)$ at $k = 0$, expressible as:

$$I_1(r) = \left(-\frac{3}{4} + q(q-1) \right). \tag{30}$$

Giving two solutions for q as $q_1 = \frac{3}{2}$ and $q_2 = -\frac{1}{2}$. The higher number may be considered to yield the first solution and, since the roots are separated by an integer, the second solution may be expressed as [50]:

$$\widehat{u_2}(\bar{r}) = Cln(\bar{r}) + \sum_{k=0}^{\infty} B_k (\bar{r}R)^{k+q_2} \ . \tag{31}$$

However, it turns out that the coefficient $C = 0$ and $B_0 = 0$ must vanish in order to satisfy the finite displacement and rotational degrees of freedom at $r = 0$, which demonstrates the uniqueness of the final solution for the transverse displacement field ($q = q_1$). Eq. (29) may be rewritten as the summation of a finite expansion of the polynomial terms as dictated by, and up to the highest degree of the function $f(\bar{r})$, together with an infinite series in terms of A_k as (Note that the term $R^{7/2}$ drops from the expression with $k = 2$):

$$\begin{aligned} &I_1(r) + \sum_{k=2}^{\infty} a_0 A_{k-2} \bar{r}^{k+q} + \sum_{k=4}^{\infty} b_0 A_{k-4} \bar{r}^{k+q} - \frac{2}{3} R^{-2} \sum_{k=6}^{\infty} b_0 A_{k-6} \bar{r}^{k+q} + \\ &\frac{1}{6} R^{-4} \sum_{k=8}^{\infty} b_0 A_{k-8} \bar{r}^{k+q} + \sum_{k=0}^{\infty} \left(-\frac{3}{4} + (k+q)(k+q-1) \right) A_k \bar{r}^{k+q} - \frac{P_0 \bar{r}^{\frac{7}{2}}}{2D_1} = 0. \end{aligned} \tag{32}$$

As the coefficients of the combined similar terms must be zero to satisfy Eq. (32), it transpires from the truncation of the series that: (i) the coefficients with odd indices vanish, and (ii) those of the even indices fit a recursive expression as:

$$A_k \left(-\frac{3}{4} + (k+q)(k-1+q) \right) + a_0 \langle A_{k-2} \rangle + b_0 \langle A_{k-4} \rangle - \frac{2}{3} b_0 R^{-2} \langle A_{k-6} \rangle + \frac{1}{6} b_0 R^{-4} \langle A_{k-8} \rangle - \frac{P_0}{2D_1} \delta_{\left(k+q-\frac{7}{2}, 0 \right)} = 0, \ k = 2, 4, 6, \cdots, \tag{33}$$

where the subscript $\langle A_{k-s} \rangle$ (whereby $s = 2,\ 4,\ 6,\ 8$ and $\langle x \rangle$ denotes Macaulay brackets) depicts a scaled Heaviside function (singularity function with order 1), expressed as:

$$\langle A_{k-s} \rangle = \begin{cases} 0, & k - s < 0 \\ A_{k-s}, & k - s \geq 0 \end{cases}, \tag{34}$$

while $\delta_{\left(k+q-\frac{7}{2}, 0 \right)}$ represents the Kronecker Delta symbol (substitution operator).

The general solution can be written as a generalised recursive formula as:

$$A_k = -\frac{\left[a_0 \langle A_{k-2} \rangle + b_0 \langle A_{k-4} \rangle - \frac{2}{3} b_0 R^{-2} \langle A_{k-6} \rangle + \frac{1}{6} b_0 R^{-4} \langle A_{k-8} \rangle \right]}{(4n(n+1))} + \frac{P_0}{2D_1 (4n(n+1))} \delta_{\left(k+q-\frac{7}{2}, 0 \right)}, \tag{35}$$

where $n = k/2$. The first three modes are expressed in (A. 2 a-c). Clearly, any mode of deformation is in tandem with its four prior modes. Although the procedure is initiated with iteration, as the expression (35) yields any mode of the transverse displacement field in its entirety, the final solution is exact and, in a similar fashion, the infinite form of the stress potential function is derived by substitution of Eq. (28) into Eq. (16) together with using Eq. (35), as exercised in §A.2. While it is also possible to, intuitively, derive a generic expression of an arbitrary mode of the transverse displacement in terms of the first component only (A_0), which may be proven by induction, the mathematical procedure turns out inherently cumbersome and fraught with difficulty, given the infinite number of modes. However, the leading terms are derived as

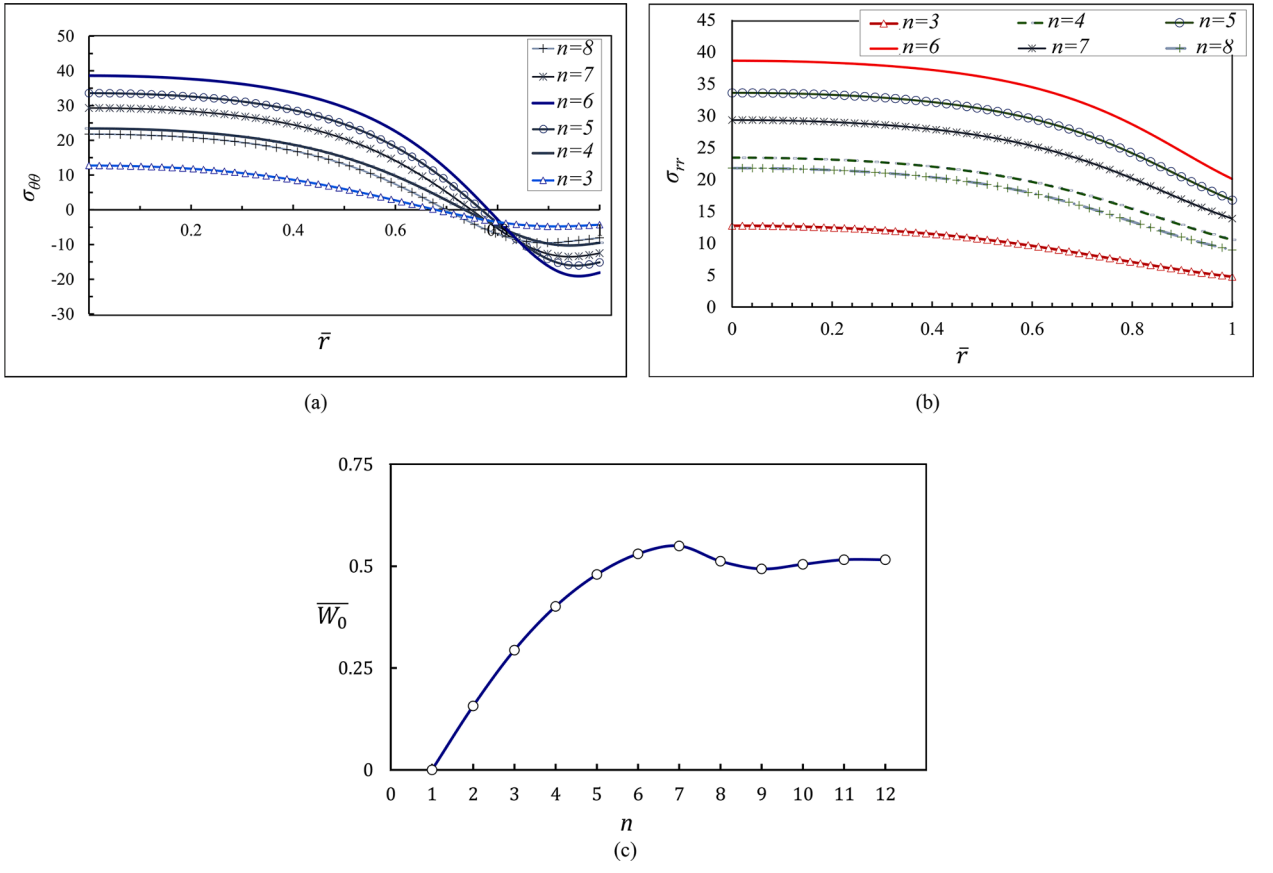

Fig. 2. variation of the circumferential (a) and radial (b) stress fields throughout the plate based on the number of modes with even indices n, while (c) represents the convergence of the midpoint displacement.

$$A_{2n} = \frac{(-1)^n a_0^n}{4^n n!(n+1)!}A_0 + \frac{(-1)^{n-1} a_0^{\langle n-1\rangle} P_0}{2\times 4^n n!(n+1)!D_1}A_0 + \frac{(-1)^{n-1} b_0 a_0^{\langle n-2\rangle}}{2n!(n+1)!}A_0 + \frac{(-1)^n \sum_{j=3}^{\infty} j(j-1)b_0 a_0^{\langle n-3\rangle}}{2\times 4^n n!(n+1)!D_1}\frac{P_0}{D_1}$$

$$-\frac{2}{3}\frac{(-1)^n \sum_{j=1}^{\infty} j^2(j+1)(j-1)b_0 R^{-2}\, a_0^{\langle n-3\rangle}}{4^{n-2} n!(n+1)!}\, A_0 + \cdots, \tag{36}$$

with n assuming natural numbers. The coefficient $c^{\langle n-j\rangle}$ obeys the condition of Eq. (34), i.e. for $n \leq j$ this term is disregarded. The first component of the displacement field, A_0 is not arbitrary and is determined by applying the Dirichlet BC's of the clamped plate at the periphery, written as in Eq. (37).

$$A_0 = -\sum_{n=1}^{\infty} A_{2n} R^{2n}, \text{ thus} \tag{37}$$

The rotational degree of freedom is therefore given as:

$$\frac{d\overline{w}(\bar{r})}{d\bar{r}} = \sum_{n=1}^{\infty} \frac{A_k}{h} R^{2n+2}\left(\bar{r}^{2n+1} - \bar{r}\right). \tag{38}$$

Integrating Eq. (38) and applying the Dirichlet's BC yields:

$$\overline{w}(r) = \sum_{n=1}^{\infty} \frac{A_{2n} R^{2n+2}}{2h(n+1)}\left(\bar{r}^{2n+2} - (n+1)\bar{r}^2 + n\right). \tag{39}$$

Eq. (39) degenerates to Eq. (22) for $n = 1$ and $a_0 = 0$. The convergence of the radial and circumferential stresses are compared in Fig. 2a-b. It can be observed from Fig. 2c that while the 6th and 7th terms contribute to an increase in the radial and circumferential stresses, convergence of midpoint displacement ($\overline{W}_0$) is satisfied considering only the first 6 terms ($A_0 - A_{10}$). The rotational DOF, however, converges at a faster rate.

4. Dynamic Response

4.1. First Phase of motion

The mathematical treatment in the case of dynamic loading dealt with is in the same fashion as outlined in the four steps stated in the case of static loads, with the use of Eq. (14), or its derivative with respect to the generalised coordinate $\bar{r}$, followed by applying the boundary and kinematic conditions. However, it is pragmatic to assume a displacement profile as derived in Eq. (39), which is truncated into a finite polynomial series. The components of each deformation mode (A_j) in Eq. (28), however, account for the temporal part of the displacement field.

The stress potential function may be treated in a similar fashion, i.e. as an infinite series. It is rather straightforward to determine the power indices of the stress potential function using the Frobenius method, as argued in Appendix A.2. Clearly, the resulting expanded series as expressed in Eq. (40) has coefficients expressing the temporal part of the stress potential.

$$\Phi(t,r) = \sum_{k=0}^{\infty} \widehat{\phi_k}(t) r^{2k}. \tag{40}$$

Following the substitution of Eqs. (40) and (28) into Eq. (13) and some algebraic manipulation a polynomial of even indices is obtained. It turns out that the coefficients of the polynomial must be all zero to satisfy Eq.(16), wherefrom the components of the Airy Stress function are expressed as

$$\widehat{\phi_n} = \frac{E}{16(n+1)^2 n}[A_0 A_{\langle 2n-2\rangle} + H(2n-4)A_2 A_{\langle 2n-4\rangle} + H(2n-6)A_4 A_{\langle 2n-6\rangle} + H(2n-8)A_6 A_{\langle 2n-8\rangle} + H(2n-10)A_8 A_{\langle 2n-10\rangle} + \cdots], \tag{41}$$

with n taking cardinal numbers. The first component of the stress potential function is thus expressed as:

$$\widehat{\phi_0} = a_1 A_2 (t)^2 + b_1 A_4(t)^2 + c_1 A_6(t)^2 + 2d_1 A_2(t)A_4(t) + 2e_1 A_2(t)A_6(t) + 2f_1 A_4(t)A_6(t). \tag{42}$$

Substituting Eqs. (40)-(41) into Eq. (14) followed by the use of Eq. (12a-e) yields as many independent PDEs as the number of modes taken into account for the displacement profile. For convenience, however, only the first three modes are assumed in the dynamic analysis. This is because the first three modes prove to accurately estimate the transient displacement field of the plate [37]. To reduce the sets of PDEs into those of ODEs, we employ the Ritz-Galerkin-Variational method to eliminate the spatial dependence of the

expressions as

$$\int_0 \left(\frac{d}{d\bar{r}} \left(\frac{d\bar{w}}{d\bar{r}} \frac{d\bar{\phi}}{d\bar{r}} \right) + \left(p - \frac{h^2}{a_s^2} \ddot{w} \right) \bar{r}^4 - \frac{1}{12(1-\nu^2)} \frac{d\mathscr{L}(\bar{w}, \bar{r})}{d\bar{r}} \right) \delta\bar{r} d\bar{r} = 0, \tag{43}$$

where the parameter $\delta\bar{r}$ is the weight function herein assumed as the spatial part of components corresponding to each mode of the displacement field.

$$ODE0 : \mathrm{R}^{10}\mu \frac{\ddot{\mathrm{A}}_2(t)}{240} + \mathrm{R}^{12}\mu \frac{\ddot{\mathrm{A}}_4(t)}{144} + \mathrm{R}^{14}\mu \frac{\ddot{\mathrm{A}}_6(t)}{112} + \frac{8\mathrm{D}_1\mathrm{R}^6\mathrm{A}_2(t)}{3} + 12\mathrm{D}_1\mathrm{R}^8\mathrm{A}_4(t) + \frac{144\mathrm{D}_1\mathrm{R}_1^{10}\mathrm{A}_6(t)}{5} - \mathrm{hG}_0(t) = \mathrm{P}_0\mathrm{R}^6 \Big/ 6, \tag{44}$$

$$ODE2 : 47R^{12}\mu \frac{\ddot{A}_2(t)}{480} + R^{14}\mu \frac{\ddot{A}_4(t)}{280} + 3R_1^{16} \frac{\ddot{A}_6(t)}{640} + 2D_1R^8A_2(t) + \frac{48D_1R^{10}A_4(t)}{5} + 24D_1R^{12}A_6(t) - hG_2(t) = P_0R^8 \Big/ 8, \tag{45}$$

$$ODE4 : R_1^{14}\mu \frac{\ddot{A}_2(t)}{840} + R_1^{16}\mu \frac{\ddot{A}_4(t)}{480} + R_1^{18}\mu \frac{\ddot{A}_6(t)}{360} + \frac{8}{5}D_1R_1^{10}A_2(t) + 8D_1R_1^{12}A_4(t) + \frac{144D_1R_1^{14}A_6(t)}{7} - hG_4(t) = P_0R_1^{10} \Big/ 10. \tag{46}$$

Now, the nonlinear function $\mathrm{G_k}$ represents the membrane stiffness of the MDOF system obtained, which consist of the multiplicative cubic terms of the modes of the transverse displacement, and is expressed in (A. 5)-(A. 7). Thus, Eqs. (44)-(46) are analogous to the undamped, forced vibrations of MDOF non-linear springs, representative of non-homogenous forms of the Duffing equation. The explicit solution of the ODEs is fraught with difficulty due to the presence of mode coupling which renders the mathematical treatment inherently complex. Therefore, approximate and numerical methods may be used to treat problems of this kind. It should nevertheless be noted that the exact solution to the expressions of this form, even for an SDOF system, entails a secular term, such as tsint, which renders the deformation non-periodic where the displacement field grows unboundedly over time. Hence, the Lindstedt-Poincaré perturbation technique is sought to eliminate the secular terms to obtain a bounded solution. To this end, each mode of the displacement field is expressed as follows:

$$A_k(\tau) = A_k^{(0)}(\tau) + \varepsilon_0 A_k^{(1)}(\tau) + \varepsilon_0^2 A_k^{(2)}(\tau) + O\left(\varepsilon_0^3\right), \tag{47}$$

$$\tau = \left(\omega_{02} + \int_0 \overline{\omega}_1 + \int_0^2 \overline{\omega}_2 + O\left(\int_0^3 \right) \right) t, \tag{48}$$

where ε_0 is a small perturbation parameter, herein related to the plate slenderness ratio defined as $\varepsilon_0 = (h/R)^4$.The frequency of vibration is scaled by the term $\overline{\omega}_1$ and $\overline{\omega}_2$ on the first and second perturbation scales, $\mathrm{A}_\mathrm{k}^{(1)}(\tau)$ and $\mathrm{A}_\mathrm{k}^{(2)}(\tau)$, respectively. These frequencies are hereafter referred to as the vibration pseudo frequencies (VPS). In what follows, the mathematical analysis, therefore, is treated in two circumstances, using the Lindstedt-Poincaré method on MDOF system as outlined in the ODEs (44)-(46) but ignoring the quadratic perturbation term (i.e. on ε_0^2) and an SDOF model by ignoring the second and third modes ($\mathrm{A}_2(t)$ and $\mathrm{A}_4(t)$, respectively) while retaining the quadratic perturbation term. Clearly,$\ddot{A}_k(t) = (\omega_{02} + \varepsilon\overline{\omega}_1)^2 \ddot{A}_k(\tau)$. Substituting these expressions in Eqs. (44)-(46), followed by the notion that each of the expressions compiled in terms of ε_0^i should be zero, yields the resulting following Nonlinear ODEs:

$$\begin{aligned} \mathrm{ODE0} : & \frac{\mu\mathrm{R}^{10}}{240}\left(2\omega_{02}\overline{\omega}_1\ddot{\mathrm{A}}_2^{(0)}(\tau) + \omega_{02}^2\ddot{\mathrm{A}}_2^{(1)}(\tau)\right) + \frac{\mu\mathrm{R}^{12}}{144}\left(2\omega_{02}\overline{\omega}_1\ddot{\mathrm{A}}_4^{(0)}(\tau) + \omega_{02}^2\ddot{\mathrm{A}}_4^{(1)}(\tau)\right) + \frac{\mu\mathrm{R}^{14}}{112}\left(2\omega_{02}\overline{\omega}_1\ddot{\mathrm{A}}_6^{(0)}(\tau) + \omega_{02}^2\ddot{\mathrm{A}}_6^{(1)}(\tau)\right) \\ & + \frac{8}{3}\mathrm{D}_1\mathrm{R}^6\mathrm{A}_2^{(1)}(\tau) + 12\mathrm{D}_1\mathrm{R}^8\mathrm{A}_4^{(1)}(\tau) + \frac{144}{5}\mathrm{D}_1\mathrm{R}^{10}\mathrm{A}_6^{(1)}(\tau) - \frac{\mathrm{hG}_0(\tau)}{\int_0} = 0, \end{aligned} \tag{49}$$

$$\begin{aligned} \mathrm{ODE2} : & \frac{\mu\mathrm{R}^{12}}{480}\left(2\omega_{02}\overline{\omega}_1\ddot{\mathrm{A}}_2^{(0)}(\tau) + \omega_{02}^2\ddot{\mathrm{A}}_2^{(1)}(\tau)\right) + \frac{\mu\mathrm{R}^{14}}{280}\left(2\omega_{02}\overline{\omega}_1\ddot{\mathrm{A}}_4^{(0)}(\tau) + \omega_{02}^2\ddot{\mathrm{A}}_4^{(1)}(\tau)\right) + \frac{3\mu\mathrm{R}^{16}}{640}\left(2\omega_{02}\overline{\omega}_1\ddot{\mathrm{A}}_6^{(0)}(\tau) + \omega_{02}^2\ddot{\mathrm{A}}_6^{(1)}(\tau)\right) \\ & + 2\mathrm{D}_1\mathrm{R}^8\mathrm{A}_2^{(1)}(\tau) + \frac{48\mathrm{D}_1\mathrm{R}^{10}\mathrm{A}_4^{(1)}(\tau)}{5} + 24\mathrm{D}_1\mathrm{R}^{12}\mathrm{A}_6^{(1)}(\tau) - \frac{\mathrm{hG}_2(\tau)}{\int_0} = 0, \end{aligned} \tag{50}$$

$$\begin{aligned} \mathrm{ODE4} : & \frac{\mu\mathrm{R}^{14}}{840}\left(2\omega_{02}\overline{\omega}_1\ddot{\mathrm{A}}_2^{(0)}(\tau) + \omega_{02}^2\ddot{\mathrm{A}}_2^{(1)}(\tau)\right) + \frac{\mu\mathrm{R}^{16}}{480}\left(2\omega_{02}\overline{\omega}_1\ddot{\mathrm{A}}_4^{(0)}(\tau) + \omega_{02}^2\ddot{\mathrm{A}}_4^{(1)}(\tau)\right) + \frac{\mu\mathrm{R}^{18}}{360\mathrm{h}}\left(2\omega_{02}\overline{\omega}_1\ddot{\mathrm{A}}_6^{(0)}(\tau) + \omega_{02}^2\ddot{\mathrm{A}}_6^{(1)}(\tau)\right) \\ & + \frac{8\mathrm{D}_1\mathrm{R}^{10}\mathrm{A}_2^{(1)}(\tau)}{5} + 8\mathrm{D}_1\mathrm{R}^{12}\mathrm{A}_4^{(1)}(\tau) + \frac{144\mathrm{D}_1\mathrm{R}^{14}\mathrm{A}_6^{(1)}(\tau)}{7} - \frac{\mathrm{hG}_4(\tau)}{\int_0} = 0. \end{aligned} \tag{51}$$

The mathematical solutions are sought in two phases of motion as follows. The first phase corresponding to a forced vibration while the loading is active, followed by phase 2 of motion whereby the loading is complete whilst the residual vibration continues.

4.2. *First Phase of motion* $(0 \leq t \leq t_d)$

4.2.1. *Single degree-of-freedom model*

For a single-degree-of-freedom system, either of the Eqs. (44)-(46) boils down to:

$$\frac{d^2A_2(t)}{dt^2} + \omega_0^2 A_2(t) + \varepsilon_0 K A_2(t)^3 = \frac{40P_0}{R^4\mu}, \tag{52}$$

Ignoring the nonlinear term, the solution is cast as $A_2^{(0)} = c_2(1 - \cos(\omega_{02}t))$, where $c_2 = \frac{P_0}{16D_1}$, when the kinematic boundary conditions of the displacement and velocity at the onset of motion are applied; while the stiffness and frequency of vibration are expressed, respectively, as:

$$K = \frac{-20Eh\left(R^6 + 84f_1\right)}{21R^2\mu\varepsilon_0}, \tag{53}$$

$$\omega_0 = \frac{8}{R^2}\sqrt{\frac{10D_1}{\mu}}, \tag{54}$$

where f_1 is expressed in (A. 8f). It should nevertheless be noted that, since both R and ν are positive, the parameter K remains positive as long as $R(\nu+1) < 4$ or $R(\nu+1) > 9.6$. For most practical applications on metal plates, $\nu \sim 0.3 - 0.33$ and thus $R < 3m$ satisfies the condition. Thus, such a system undergoes elastic hardening. Conversely, in the case of $K < 0$ elastic softening is observed. Chaotic dynamic motion occurs when viscoelastic and/or temperature effects are taken into account [27, 33, 38, 51, 52].

By adjusting the displacement and time from the Lindstedt-Poincaré technique Eqs. (47)-((48)), the nonlinear ODEs in order of the perturbation parameter ε_0 are expressed as

$$\varepsilon_0\left(\omega_0^2\left(A_2(\tau)^{(1)} + \ddot{A}_2(\tau)^{(1)}\right) + 2\omega_0\overline{\omega}_1\ddot{A}_2(\tau)^{(0)} + K\left(A_2(\tau)^{(0)}\right)^3\right) = 0 \tag{55}$$

$$\varepsilon_0^2\left(\omega_0^2\left(\ddot{A}_2(\tau)^{(2)} + A_2(\tau)^{(2)}\right) + 2\omega_0\overline{\omega}_2\ddot{A}_2(\tau)^{(0)} + 2\omega_0\overline{\omega}_1\ddot{A}_2(\tau)^{(1)} + \overline{\omega}_1^2\ddot{A}_2(\tau)^{(0)} + 3K\left(A_2(\tau)^{(0)}\right)^2A_2(\tau)^{(1)}\right) = 0, \tag{56}$$

where $\overline{\omega}_1$ and $\overline{\omega}_2$ represent the perturbation frequencies as defined earlier. Interestingly, considering now the second mode (replacing $A_2(t)$ by $A_4(t)$) individually, the values above refurnish into $\omega = \sqrt{1728D_1}/R^4\mu$ and $K = -(25ER^{10} + 1536d_1)/(20R^2\rho\varepsilon_0)$, where d_1 is expressed in (A. 8d), while the ODEs above still remain valid. The expression containing the first perturbation term $A_2(\tau)^{(0)}$ leads to the linearised solution as discussed earlier (with $\varepsilon_0 = 0$). The solution to Eq. (55) is expressed as:

$$A_2^{(1)}(\tau) = \left(-\frac{c_2\overline{\omega}_1}{\omega_0} + \frac{15c_2^3K}{8\omega_0^2}\right)\tau\sin(\tau) - \frac{c_2\cos(\tau)\omega_{12}}{\omega_0} + E_1\sin(\tau) + E_2\cos(\tau) + \frac{c_2^3K(-\cos^3(\tau) + 8\cos^2(\tau) + 15\cos(\tau) - 24)}{8\omega_0^2}. \tag{57}$$

With $E_1 = 0$ and $E_2 = c_2(c_2^2K + 4\omega_0\overline{\omega}_1)/(4\omega_0^2)$. The value of $\omega_{12} = 15c_2^2K/(8\omega_{02})$ eliminates the secular terms. Hence, Eq. (57) is furnished into

$$A_2^{(1)}(\tau) = \frac{c_2^3K((1-\cos(\tau))(\cos^2(\tau) - 7\cos(\tau) - 24))}{8\omega_0^2}. \tag{58}$$

Similarly, the solution to Eq. (56) is given as

$$A_2^{(2)}(\tau) = -\frac{c_2\left(2565c_2^4K^2 + 256\omega_0^3\overline{\omega}_1\right)\tau\sin(\tau)}{256\omega_0^4} + F_1\cos(\tau) + F_2\sin(\tau) - \frac{c_2^5K^2}{256\omega_0^4}\left(4\cos^5(\tau) - 64\cos^4(\tau) - 125\cos^3(\tau) + 2624\cos^2(\tau) + 2565\cos(\tau) - 5632 + \frac{256\cos(\tau)\omega_{02}^3\overline{\omega}_2}{c_2^4K^2}\right), \tag{59}$$

where $F_1 = (c_2(64\omega_0^3\overline{\omega}_2 - 157c_2^4K^2))/(64\omega_0^4)$ and $F_2 = 0$, derived from the kinematic condition of the displacement and velocity at the onset of loading, respectively, and further reduced by using the expression of first vibration pseudo frequency. The second one is derived as $\overline{\omega}_2 = -2565c_2^4K^2/(256\omega_{02}^3)$.

4.2.2. *Multiple Degree-of-freedom model*

Neglecting the nonlinear terms of Eqs. (44)-(46), an ansatz for the displacement components $A_i(t)$ in each of the linearised ODEs

may be either intuitively expressed as $A_k(t) = a_k \sin(\omega_{0k} t) + b_k \cos(\omega_{0k} t) + c_k$, or derived using the Laplace transform, which, by applying the same kinematic conditions at the onset of loading, boils down to

$$A_k(t) = c_k(1 - \cos(\omega_{0k} t)) \tag{60}$$

Substituting Eq. (60) in the ODEs (44)-(46) and ignoring the nonlinear functions G_k yields three simultaneous expressions in terms of c_k. It turns out that these ODEs and their time derivatives must be satisfied, at every instant of time, to ensure the energy equilibrium of the plate. Thus, at the onset of loading, it turns out from the solution of the three simultaneous ODEs that the amplitudes of the displacement function read:

$$c_2 = 4200 \frac{P_0}{R^4 \mu \omega_{02}^2}, \tag{61}$$

$$c_4 = -6384 \frac{P_0}{R^6 \mu \omega_{04}^2}, \tag{62}$$

$$c_6 = 3024 \frac{P_0}{R^8 \mu \omega_{06}^2}. \tag{63}$$

The frequencies ω_{0k} are determined by substitution of Eqs. (60)-(63) into the ODEs (44)-(46) followed by a differentiation with respect to time twice. The equilibrium at the onset of loading yields:

$$\omega_{02} = \frac{2596.29}{5} \sqrt{\frac{D_1}{R^4 \mu}}, \tag{64}$$

$$\omega_{04} = 515.58 \sqrt{\frac{D_1}{R^4 \mu}}, \tag{65}$$

$$\omega_{06} = 512.37 \sqrt{\frac{D_1}{R^4 \mu}}. \tag{66}$$

Alternatively, by applying Laplace transform on the ODEs (44)-(46) we arrive at identical expressions for the amplitude and frequencies of modal vibrations above. Eq. (60) and its second time derivative may be integrated into Eqs. (49)- (51) as $A_k^{(0)}$, leading to coupled forced vibrations of the MDOF system. Due to the interdependence of these expressions, the mathematical treatment of the nonlinear ODEs (49)-(51) is sought numerically using ODE45. In the absence of the closed-form solution and by using the perturbation techniques, however, only approximate values for ϖ_1 and hence the displacement fields can be sought to diminish the unbounded amplitude growth over time whereby harmonic vibration is attained. It should be however recognized that, considering the duration of the pulse pressure is infinitesimal, there is only marginal growth of the displacement field over time in the first phase while the load lasts, and the linear and nonlinear solutions are close at this stage [37]. The major influence of the pressure occurs due to the residual stresses accumulated in the plate in the next phase of motion.

4.3. *Second phase of motion* $(t \geq t_d)$

The loading is complete at time $t = t_d$; but at the moment of the pulse termination, the system possesses kinetic and strain energies thus retains its motion due to the initial inertia effects and the elastic energy stored in it. Thus, following the forced vibration from phase one of motion, a free vibration governs the response of the plate. At the offset of the loading duration, the kinematic continuity applies to ensure there are no displacement or velocity jumps throughout the motion.

The analysis in this phase is carried out in the same spirit as the previous phase of motion- with the solution of linear and nonlinear parts of the displacement field determined, respectively. By disregarding the nonlinear terms, the first iteration of ODE is expressed, for SDOF and MDOF models as follows.

4.3.1. *SDOF Model*

Using the kinematic continuity of displacement and velocity fields, the solution to Eq. (52) is:

$$A_2(\tau) = c_2(\cos(\tau - \tau_d) - \cos(\tau)), \tag{67}$$

where $\tau_d = \omega_{02} t_d$ is the dimensionless duration. Substituting Eq. (67) in Eqs. (55)-(56) and performing some algebraic manipulations, the solution to the next perturbed terms of displacement field are furnished as:

$$A_2^{(1)}(\tau) = E_3\cos(\tau) + E_4\sin(\tau) + \left[\begin{array}{l} \dfrac{3\tau c_2}{4\omega_{02}^2}(\sin(\tau)-\sin(\tau-\tau_d))\left(c_2^2K(\cos(\tau_d)-1)-\dfrac{4}{3}\omega_{02}\overline{\omega}_1\right)+\dfrac{(\cos(\tau-\tau_d)-\cos(\tau))\overline{\omega_1}}{2\omega_1}+\dfrac{c_2^3K}{32\omega_{02}^2} \\ (-\cos(3\tau-3\tau_d)+3\cos(3\tau-2\tau_d)-3\cos(3\tau-\tau_d)+18\cos(\tau-\tau_d)-6\cos(\tau-2\tau_d)+6\cos(\tau+\tau_d)+\cos(3\tau)-18\cos(\tau)) \end{array}\right]. \tag{68}$$

The magnitude of the pseudo frequency is evaluated such as to eliminate the secular term in the first set of brackets (i.e. the terms involving $\sin(\tau) - \sin(\tau - \tau_d)$):

$$\overline{\omega}_1 = \frac{3c_2^2K}{4\omega_{02}}\ (1-\cos(\tau_d)). \tag{69}$$

In a similar fashion to the linearised solution (with $\varepsilon_0 = 0$), applying the kinematic continuity of the displacement field leads to the integration constants as:

$$E_3 = \frac{-c_2^3K}{16\omega_{02}^2}\left(10cos^3(\tau_d)+3cos^2(\tau_d)+24\cos(\tau)-37\right), \tag{70}$$

$$E_4 = \frac{-c_2^3K}{16\omega_{02}^2}\sin(\tau_d)\left(10cos^2(\tau_d)+3\cos(\tau_d)+47\right). \tag{71}$$

Substituting Eqs. (67)-(69) in Eq. (56), the solution to $A_2^{(2)}(\tau)$ is determined as:

$$\begin{aligned} A_2^{(2)}(\tau) &= f\left(\overline{\omega}_2\right) + F_3\cos(\tau) - F_4\sin(\tau) + \frac{c_2\overline{\omega}_{22}(\cos(\tau-\tau_d)-\cos(\tau))}{2\omega_{02}} - \frac{3Kc_2^3}{32\omega_{02}^2}(-12\cos(\tau)+12\cos(\tau-\tau_d)-4\cos(\tau-2\tau_d) \\ &-3\cos(3\tau-\tau_d)+3\cos(3\tau-2\tau_d)-\cos(3\tau-3\tau_d)+4\cos(\tau+\tau_d)+\cos(3\tau)) \\ &-\frac{K^2c_2^5}{1024\omega_{02}^4}\Big(444\cos(\tau)+\cos(5\tau)-165\cos(3\tau)-444\cos(\tau-\tau_d)+222\cos(\tau-2\tau_d)+267\cos(3\tau-\tau_d)-225\cos(3\tau-2\tau_d) \\ &+81\cos(3\tau-3\tau_d)-222\cos(\tau+\tau_d)+30\cos(\tau+2\tau_d)-30\cos(\tau-3\tau_d)+18\cos(\tau+3\tau_d)+51\cos(3\tau+\tau_d)-18\cos(\tau-4\tau_d) \\ &-6\cos(\tau+4\tau_d)+6\cos(\tau-5\tau_d)-6\cos(3\tau+2\tau_d)-5\cos(5\tau-\tau_d)+9\cos(3\tau-4\tau_d)+10\cos(5\tau-2\tau_d)-15\cos(3\tau-5\tau_d) \\ &-10\cos(5\tau-3\tau_d)+3\cos(3\tau-6\tau_d)+5\cos(5\tau-4\tau_d)-\cos(5\tau-5\tau_d)\Big), \end{aligned} \tag{72}$$

where

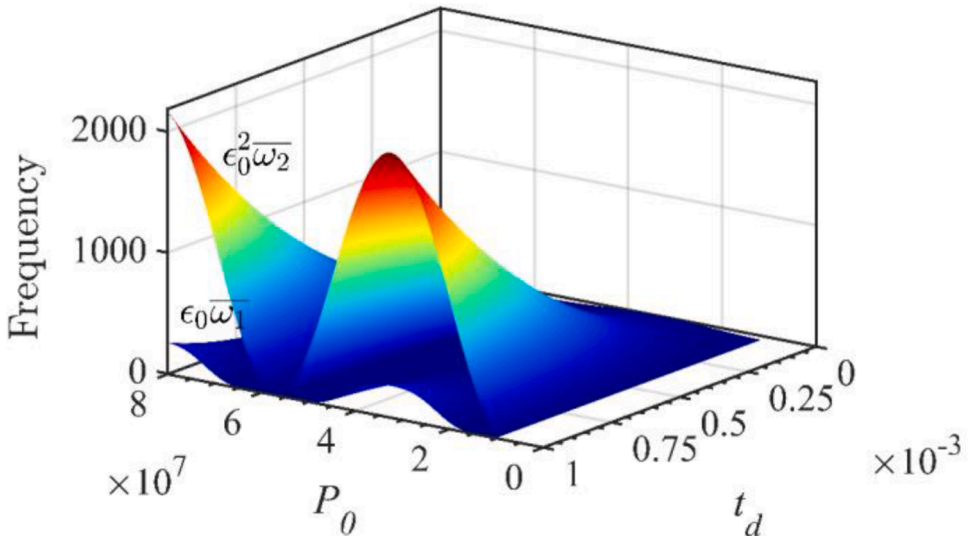

Fig. 3. Influence of the load duration and magnitude on the variations of the pseudo frequencies.

$$F_3=\frac{1}{256\omega_{02}^4}Kc_2^3(\cos(\tau_d)-1)\begin{pmatrix}48Kc_2^2\cos^5(\tau_d)-308K\cos^4(\tau_d)c_2^2-342c_2^2K\cos^3(\tau_d)+2553c_2^2K\cos^2(\tau_d)-192\cos^3(\tau_d)\omega_{02}^2+2627c_2^2K\cos(\tau_d)\\+96\cos^3(\tau_d)\omega_{02}^2+3252Kc_2^2+240\cos(\tau_d)\omega_{02}^2-144\omega_{02}^2\end{pmatrix}, \tag{73}$$

$$F_4=\frac{1}{256\omega_{02}^4}Kc_2^3\sin(\tau_d)\begin{pmatrix}48Kc_2^2\cos^5(\tau_d)-356K\cos^4(\tau_d)c_2^2+38c_2^2K\cos^3(\tau_d)+2383c_2^2K\cos^2(\tau_d)-192\cos^3(\tau_d)\omega_{02}^2+114c_2^2K\cos(\tau_d)+288\cos^2\\(\tau_d)\omega_{02}^2+5603Kc_2^2-144\cos(\tau_d)\omega_{02}^2+48\omega_{02}^2\end{pmatrix}, \tag{74}$$

and

$$f\left(\overline{\omega}_2\right)=\frac{K^2c_2^5}{64\omega_{02}^4}\left(12\cos^4(\tau_d)-12\cos^3(\tau_d)-33\cos^2(\tau_d)+54\cos(\tau_d)-21-\frac{96\cos(\tau_d)}{Kc_2^2\omega_{02}^2}+\frac{96}{Kc_2^2\omega_{02}^2}-\frac{64\omega_{02}^3\overline{\omega}_2}{K^2c_2^4}\right)\tau(\sin(\tau_d-\tau)\ +\sin(\tau)) \tag{75}$$

Through some algebraic manipulations, a closed-form solution for the parameter $\overline{\omega}_2$ is determined as:

. (76)

A comparison between the first and second VPS is visualised in Fig. 3. Clearly, the thickness of the plate plays a significant role in determining the curvature of the $\overline{\omega}_2$ function, with elevated number of local maxima as the quotient of the plate radius to its thickness increases beyond 0.13 (Fig. 4). The transient deformation of an SDOF model is plotted in Fig. 5 against the dimensionless time.

4.3.2. MDOF Model

The nonlinear ODEs in Eqs. (49)- (51) remain valid during the second phase. Using the mathematical treatment as outlined earlier, with $P_0 = 0$, the linearised solution is derived as:

$$A_k(\tau) = c_k(\cos(n_k(\tau-\tau_d))-\cos(n_k\tau)), \tag{77}$$

with $n_k = \omega_{0k}/\omega_{02}$. Substituting Eq. (77) in Eqs. (49)- (51) and using Eqs. (61)- (66), the solution to the coupled ODEs is sought numerically using ODE45, while the kinematic continuities of the transverse displacement and velocity are imposed. The parameter $\overline{\omega}_1$ is increased iteratively to harmonise the final solution.

4.4. Numerical simulations and validations

A number of Finite Element models have been set up and run in ABAQUS® Explicit 2018 to validate the analytical models of the present work. Two types of FE analyses representative of free air blast have been developed, viz. a full 3D pure Lagrangian technique and a full 3D Coupled Eulerian-Lagrangian technique. The objectives of the pure Lagrangian technique-based analyses are two-fold, the former served as a convergence study with two goals: (i) to investigate the mesh sensitivity, and (ii) to determine the influence of element type on the captured stress path and maximum displacements as primary results of plate response. The latter technique was based on a parametric study to validate the analytical model without the incorporation of the FSI phenomenon, such as deterministic loading types.

The second FE technique utilises the Multi-Material Arbitrary Lagrangian-Eulerian (MMALE) formulation to simulate the pressure-

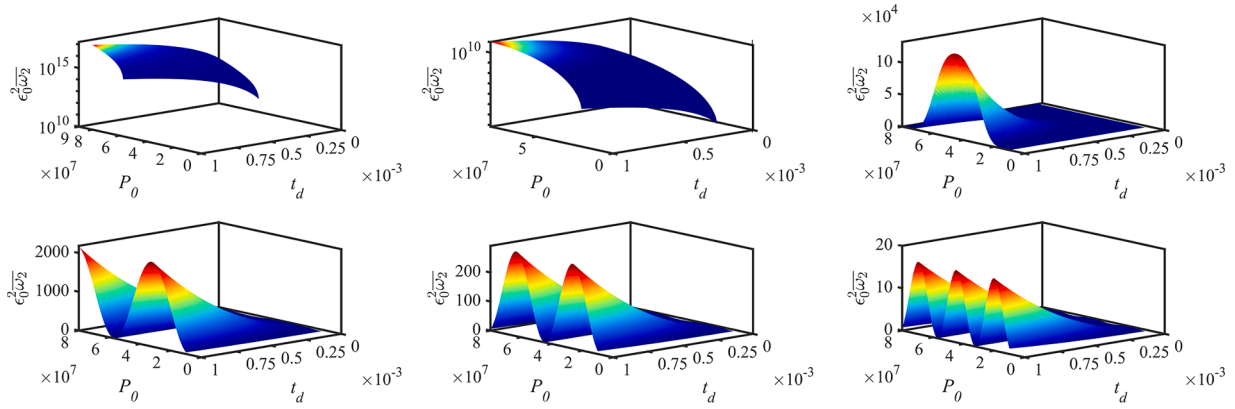

Fig. 4. Influence of the plate thickness, pressure $P_0[Pa]$ and loading duration $t_d[s]$ on the variations of the second VPS for the plate of $r = 150$ *mm*.

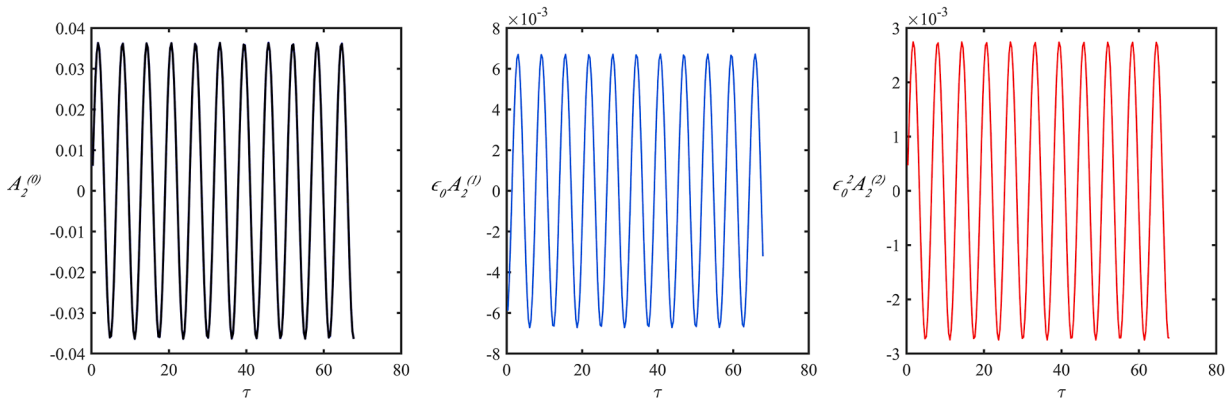

Fig. 5. Transient deformation of the plate centre for SDOF model (a) linearised (b)-(c) nonlinear components.

induced from Fluid-Structure Interaction (FSI). Practical examples of such scenarios include blast phenomena and pressure vessel explosions. The MMALE methods offer more accurate predictions of the structural response than those of the pure Lagrangian one [53].

The plates in both techniques were made of 4mm thick, purely elastic, ultra-hard ARMOX 440T steel alloy, having a density of 7850 kg.m^{-3}, radius of 150mm, Poisson's ratio of 0.28 and Young's modulus of 194GPa.

4.4.1. Pure Lagrangian model

This technique offers reduced computational time due to simplifications in the geometry and loading techniques. However, the numerical calculations of such technique should be couched in caveats due to the impulse reductions and pressure recirculation associated with the fluid-structure interactions in, say, physical blast phenomena. Often, the estimated pressure utilised in the pure Lagrangian model should be reduced on account of structural flexibility and the FSI effects [6, 41, 53, 54].

The convergence study was carried out on circular plates of a 200mm radius, clamped along the periphery. All models were subjected to a prescribed 20MPa uniform pressure for a duration of 50μ.s. The study entailed four different element types, continuum shell elements (SC8R), conventional shell elements (S4R), continuum (brick) elements (C3D8R) and membrane elements (M3D4R). Other element formulations using extended FE and super-elements to address the dynamic and shock response of beam and plate elements have been proposed [55, 56], including the novel FE super-element formulations to simulate the shock response of the heterogenuous perfoated 2D lattice systems- representative of hybrid joints [57]. The frequency analysis of such systems was performed using Floquet-Bloch's principle for lattices and the conventional FE elements, however, here the study considers the blast response of monolithic plates.

The S4R elements are general-purpose, doubly curved reduced integration shell elements with finite membrane strains and hourglass control to avoid spurious zero-energy modes. These elements allow for finite membrane strains and arbitrary large rotations. In the current study, 5 Simpson points of integrations through the plate thickness were used. On the other hand, the SC8R mesh entailed 8-noded hexahedral elements for general shell-like structures with continuum topology. Adaptable to thick and thin shells, these elements permit the analyses involving large strains with accuracy in contact pairs' investigations. The C3D8R continuum elements are a class of solid elements with reduced integration, commonly referred to as 'brick' elements. These elements require refinement to capture stress components at boundaries, while a sufficient number of them through the thickness of the plate/shell are required to provide bending stiffness. Five elements per thickness in conjunction with hourglass control were utilised for these models. The membrane elements (M3D4R) are 4-noded quadrilateral elements with reduced integration and hourglass control, which conform to simplified shell theory in which internal bending moments are neglected.

The spectrum of the mesh model was varied from the coarse-40mm element size to a fine mesh of 3mm element length, to provide element length-to-thickness ratio in descending order of 10, 5, 2.5, 1.25 and 0.6.

The convergence of displacements was guaranteed with element length of the order less or equal to the thickness of the plate for all element types. However, the shell elements converged more rapidly with smooth variation in midpoint displacements, while the results with brick elements deviated significantly with coarse meshes when the element length/thickness ratio exceeded 2.5 (Fig. 6). It should be noted that while both continuum shell elements and conventional shell elements provide the most accurate results, the conventional shell elements were chosen in this study due to the less allocated time associated with the modelling and simulation. Furthermore, the model with the finer mesh discretisation of SC8R elements took longer to run than other models. The use of brick elements increased computational time for the same level of accuracy sought (Table 1). It thus turns out the S4R elements are the most consistent element types, which are ideal candidates for the Coupled Eulerian-Lagrangian analyses.

The stress paths across the plate followed a similar trend for all element types except the membrane elements which exhibited uniform, high stress accumulation throughout the plate ascribed to its formulation as a membrane. The stress concentration at the boundaries of shell and brick elements are due to the boundary effects.

Concerning the validation of the analytical model using pure Lagrangian analysis, a uniformly distributed load was prescribed with variable magnitudes of $P_0 = 1,2,5,10,15,\ 20$ MPa with a rectangular pulse shape of duration $t_d = 50\mu$s, on the target plate which had

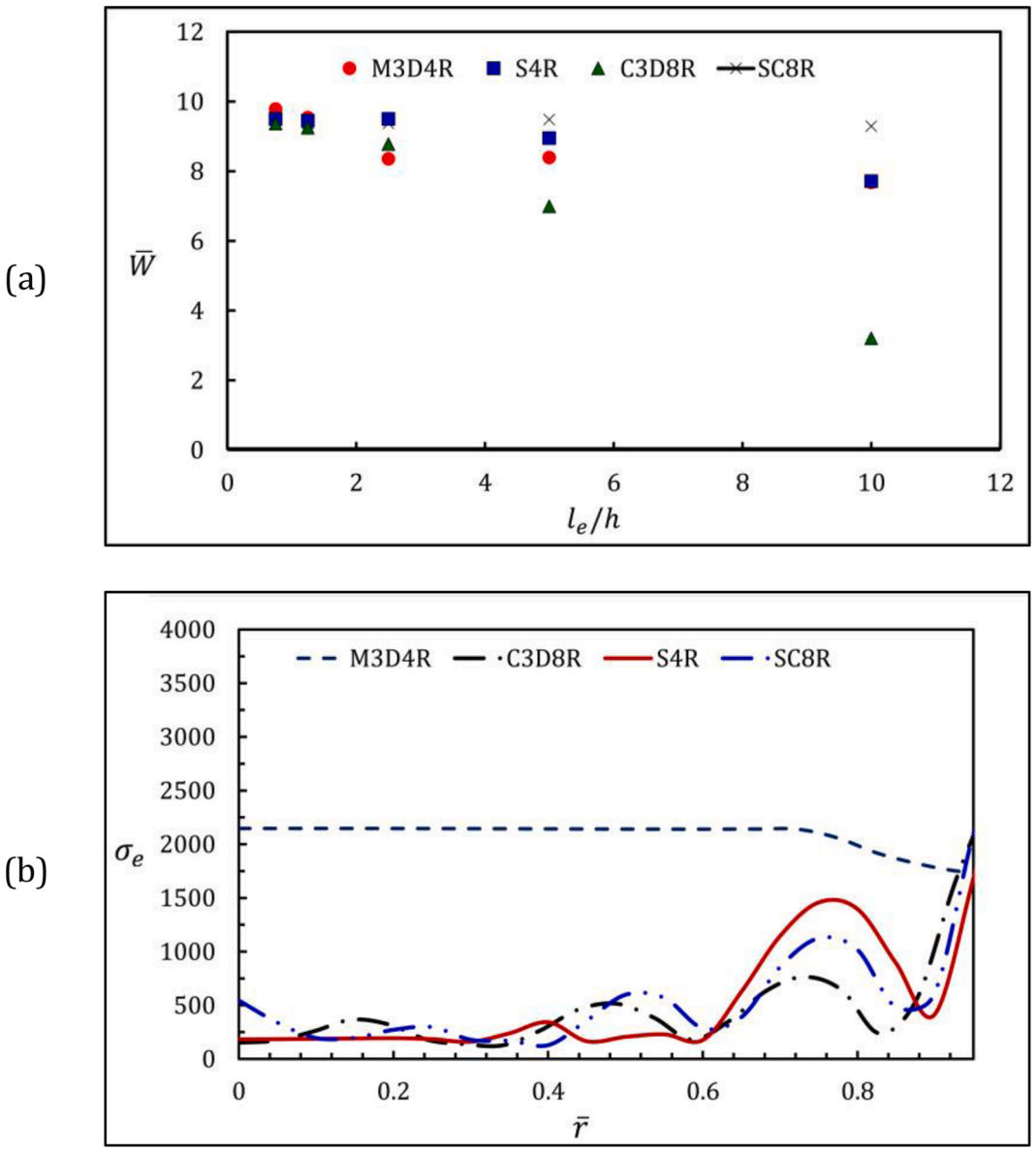

Fig. 6. (a) Comparison of the peak normalised Midpoint displacement convergence for various element types with the abscissa term l_e representing element length, (b) the equivalent Mises stress σ_e paths across the plate radial distance at 105μs

Table 1
Comparison of the analysis duration for various element types. The analyses were performed on a 2.3GHz processor with a 2.9Ghz frequency.

Element length/thickness	0.75	1.25	2.5	5	10
Element type	Analysis Duration				
M3D4R	00:04:39	00:02:25	00:00:54	00:00:37	00:00:36
C3D8R	00:12:46	00:05:55	00:0149	00:00:43	00:00:14
S4R	00:05:56	00:01:29	00:00:36	00:00:30	00:00:09
SC8R	00:24:24	00:05:52	00:02:25	00:01:03	00:00:31

various thicknesses of h = 1, 2, 5, 10, 20, 40 mm and constant radius R = 150 mm. Although the approach yields a total of 36 models for investigation, any analysis which yielded the maximum peak deformation over ten-fold of the plate thickness was discounted as it violates the assumption of large deformation-moderate strains of the FVK model. Fig. 7 compares the analytical and numerical FE models. Clearly, the plate thickness has a significant influence on the predicted peak deformations of the plate (Fig. 7b). For the plate thickness-radius ratio of more than 0.13, the peak transverse displacement depreciates below half the plate thickness, a limit wherein

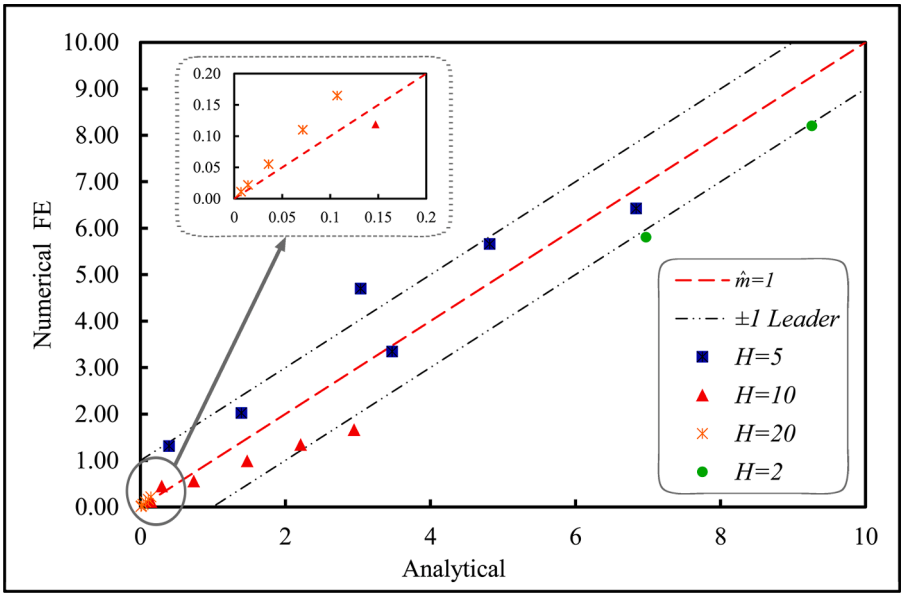

Fig. 7. (a) Deviation of the analytical model results from the Numerical FE pure Lagrangian ones (without the FSI effects). The dashed red line has a slope $\hat{m} = 1$ and highlighted with ∓ 1 leader. (b) surface interaction of the influence of the plate thickness and load magnitude on the peak deformations

the classic analytical analysis of linear dynamics satisfy accurate estimates, and the influence of the finite displacements, or geometry changes, can be ignored. Below this limit, the variation of the peak displacement with the pressure and plate thickness is rather smooth. Conversely, the resulting transverse deformation of the plates of a radius exceeding the upper limit 100% of its thickness varies abruptly with the slight change in the pressure and/or plate thickness.

4.4.2. MMALE technique

In the MMALE analysis considering the free air blast, the multi-materials (air and the explosive) were embedded in an Eulerian 500 mm high, square base cuboid with 150mm side length. To model the pulse pressure, a PE4 (of TNT equivalent yield of 1.15-1.4) explosive was placed at the bottom of the Eulerian model. The explosive was square-based cuboids of side lengths 50 and 75mm with heights varying from 5mm to 20mm, as reported in Table 2. Cubic geometry was preferred to the cylindrical one for the enhanced uniformity of mesh and the transfer of the state variables throughout the medium.

The Eulerian medium is fixed in space. The medium was discretised with EC3D8R hexahedral elements, with a constant element length of 4mm throughout, providing a sufficient number of elements to account for the fraction of the Eulerian medium that the explosive occupies. Transmission boundaries at the top and back sides of the Eulerian medium were prescribed with flow-out boundary conditions, while the other faces were adjusted with symmetric boundary conditions. The inflow of pressure was through the bottom face where the PE4 charge was modelled. A non-reflecting boundary condition was applied to this face. The schematic of the CEL model is presented in Fig. 8.

The density of PE4 and air materials were 1601kg.m^{-3} and 1.293 kg.m^{-3}, respectively. The Jones Wilkins Lee (JWL) and Ideal gas equations of state (EoS) were prescribed to the PE4 and air materials, respectively. A value of 18.27μ.Pa.s was prescribed for the viscosity of air, while the ideal gas constant of R* = 287J/kgK was used. The reader is referred to Ref. [53] for full details of the EoS data and material properties.

As the explosive product detonates instantaneously, the gaseous detonated products generated by the contact between the detonation front and the unreacted explosive material, flow through the mesh points of the reference Eulerian frame through a monotonic advection [58]. Upon contact with the plate mesh points, defined by the Lagrangian formulation, the FSI algorithms are invoked at the contact interface of the target and explosive products (which are assumed to interact in a frictionless manner) to characterise the

Table 2
Estimated pressure and charge properties of the designated models

Charge height (h_e)	5	7.5	10	15	20
Charge width L_e (mm)	75	75	50,75	50	50
Charge mass M_e (g)	180.11,	270.17	125.74, 360.23	188.61	320.20
Scaled distance Z(ft / $\sqrt[3]{\text{lb}}$)	1.67	1.46	1.73, 1.32	1.51	1.38
Overpressure p_s (MPa)	16.06	22.75	15.18, 31.03	20.68	26.20

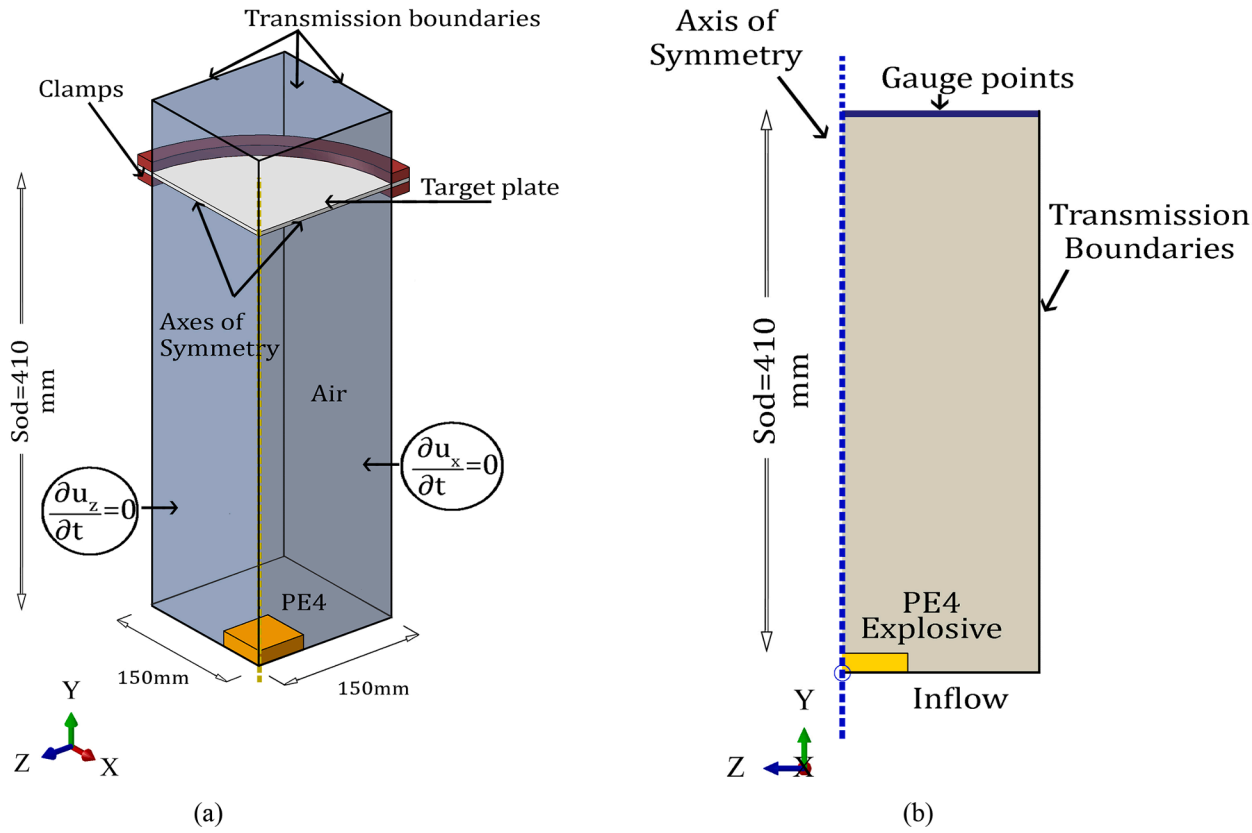

Fig. 8. Schematic of MMALE model with (a) a flexible target (CEL) and (b) rigid target.

motion of the target [18, 43, 53]. For light plates, an instantaneous gain in acceleration is followed due to the imbalance between the higher reflected pressure at the contact interface of the target front face and the fluid.

The circular plates had a radius of 170mm, were made of 4mm thick ARMOX440 steel with E = 194GPa, $\nu = 0.28$ and were discretised with S4R elements with element length to thickness ratio of unity. The plate was tied with two circular- cylindrical rigid clamps of length 20mm, bulging out of the two edges of the Eulerian medium, and height of 10mm (Fig. 8), leaving 150mm as the exposed radius of the plate. A penalty contact of 0.3 friction coefficient was prescribed for the contact surfaces between the plate and the clamps. The plate was fixed at a distance of 425mm from the inflow surface of the Eulerian medium. While the standoff distance (SOD)varies slightly due to the variation in charge's height, given the ratio of the standoff to characteristic charge diameter(length) exceeds three, the pressure may be assumed to vary uniformly across the target (case of global blasts) [59, 60]. Due to the influence of the FSI, light plates such as the one assessed here equilibrates instantaneously thus reducing the transmitted impulse. To consider pressure recirculation and to account for the FSI effects on reducing the impulse imparted to the plate, Eq. (1) together with the results of [40, 42, 43] were employed.

Using the UFC code on spherical TNT air blast with a priori knowledge of the Hopkinson-Cranz scaled distance, the reflected pressure and impulse may be estimated. A TNT equivalency of 1.37 was assumed [61]. It was further assumed that the geometry of the charge would not affect the impulse imparted given the equivalent mass of the PE4 charges and that of the spherical TNT are the same, although the distributions of pressure may vary [18, 62]. For comparison, two MMALE models with rigid target boundaries were investigated to determine the pressure distribution and the generated impulse. The charge of the model was cuboid of 50mm square-based length and charge height of 15mm, while the second one had charge dimensions of 75mm × 75mm × 7.5mm. The standoff distance was the same as the CEL counterparts.

As shown in Fig. 9a, except for the accentuated difference in the pressure distribution near the periphery of the plate ($r/R \geq 0.8$), the distribution of pressure across the plate remains moderately constant and therefore may be presumed as uniform. The pressure build-up occurring around the boundaries is due to the pressure accumulation from fluid advection transversely, combined with the reflected pressure near the centre of the target surface which travels horizontally across the contact interface. This effect leads to the clearing of the blast wave, which is driven by the diffraction of the pressure wave due to the imbalance between the reflected pressure and the incident pressure rendering the diffraction to set up flow around the target periphery [5]. Around target edges, the diffraction of the blast wave occurs due to the imbalance of the two pressure gradients, namely the higher reflected pressure on the target front face and the lower incident pressure around the target edge [9].

The impulse density (impulse per unit area) of the two models are compared in Fig. 9b.

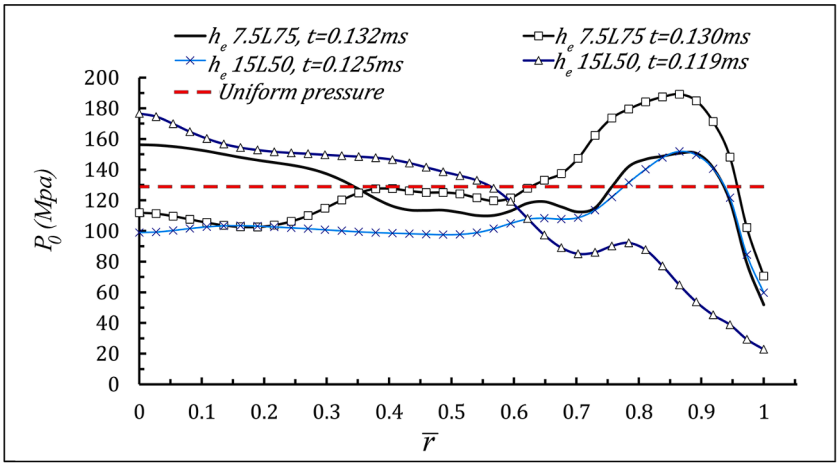

(a)

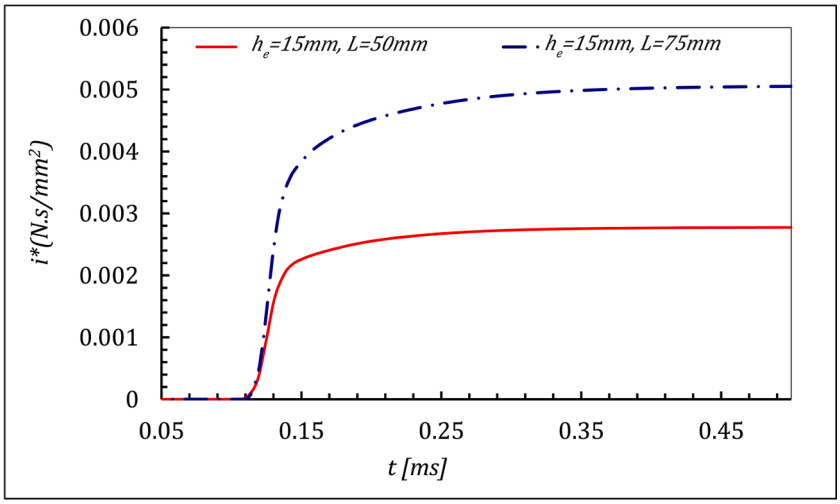

(b)

Fig. 9. (a) Distribution of the instantaneous pressure from the gauge points across the target plate, compared against the uniformly distributed pressure pulse, while (b) draws a comparison of the impulse density i^* (impulse per unit area) induced by cuboid charges of 50mm and 75mm lengths. The first and second parameters of the legend in (a) represent the explosive height h_e and the length of the charge L, respectively.

The numerical FE results as well as a comparison of the analytical SDOF model with the numerical one is illustrated in Fig. 10. The midpoint transient deformation of the plate subjected to the loading from 180g charge ($L_e = 75\text{mm}, h_e = 5\text{mm}$) is also compared against the MDOF model in Fig. 11, and due to loading from $L_e = 50\text{mm}$ and $h_e = 10\text{mm}$. With a value of $\overline{\omega}_{12} = 2.66 \times 10^5$, the deformations become harmonic and the peaks of the transient displacement are normalised.

As observed, the Numerical FE results compare favourably against the Analytical models with the MDOF system. Clearly, the major contribution to the midpoint displacement of the plate arises from the first (fundamental) mode while the higher modes $A_4(t)$ and $A_6(t)$ have a less pronounced effect on the total displacement. Thus, the mathematical treatment with three degrees of freedom can accurately estimate the response of the plate. With the inclusion of higher modes, the average peaks of the deformation field reduce. The averages of the peaks in the midpoint displacement curves are compared in Fig. 10c and the plate profile at the second maximum peak is illustrated in Fig. 10d. With the increase in the charge height, a bulging occurs above the conical profile of the plate similar to the cases of localised blasts, while becoming more discernible with the increase of the charge height to 10mm. It is recognised that the generated pulses from the presumed charge configuration induce significant peaks in the displacement time history. It should however be emphasised that, by considering high strength armour steel materials, the material response is rendered purely elastic and plastic deformation would not occur. To examine the realistic elasto-plastic response, the results can be coupled with those of the rigid, perfectly plastic plates [63-67]. The reader is referred to the Ref.'s [68, 69] for the methods of combining the two. The reselastic load-deformation curves for a structure made of an elasto-plastic material may thus be idealised by separation of the two into an initial elastic response, followed by a perfectly plastic one. The validity of the mathematical model at such amplified deformations further demonstrates the capability of the FVK expressions and, in turn, the derived theoretical solutions, to predict a wide spectrum of the

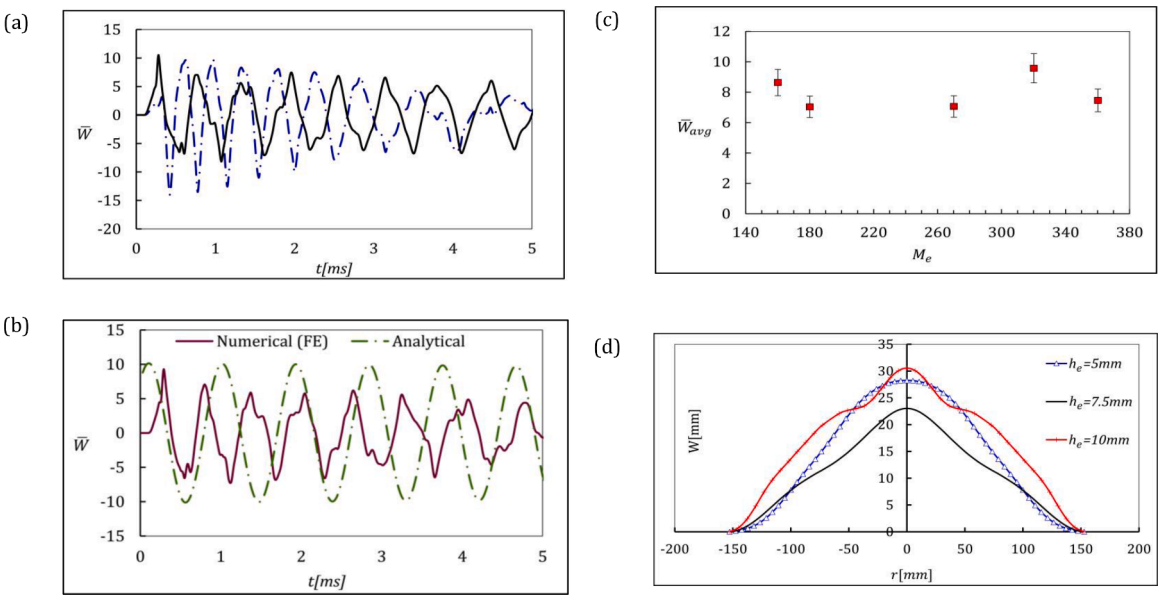

Fig. 10. (a) Transient deformation of FE models at the plate centre $\overline{W}$, with $L_e = 75$mm and 10mm $h_e = 10$mm (broken lines) against the model with $L_e = 50$mm and $h_e = 10$mm (solid line), with FSI coefficient 0.73, (b) validations of the analytical SDOF model against FE model with 22.75MPa unadjusted overpressure, (c) numerical FE results of average peaks of the midpoint displacement $\overline{W}_{avg}$ against the charge mass. The plate profiles of the models are presented in (d)

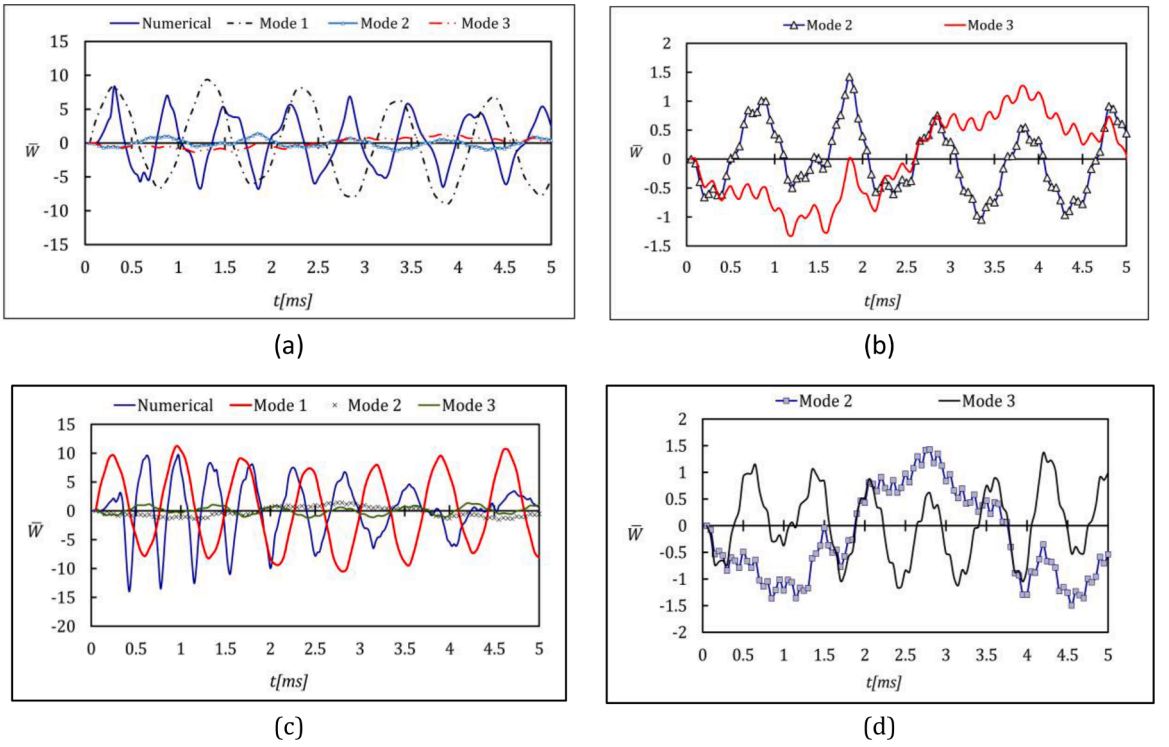

Fig. 11. Comparison of the first three fundamental modes of the analytical MDOF model with the numerical FE one for (a) $h_e = 7.5$mm and (c) $h_e = 10$mm, as well as the transient deformation of the associated higher modes from analytical model shown in (b) and (d), respectively.

transient deformations due to pulse pressure loading for practical applications.

The differences between the peaks at some points, as well as the frequency of vibrations, may be due to the factors as follows. First, in the analytical model, a rectangular profile was prescribed to the pulse shape (representing impulsive loading), while the

aforemonitored pulse shape from the FE models was exponential. It has been argued that [6, 53], in some circumstances of the distal blasts, the pressure load is deemed as dynamic, rather than impulsive, leading to the significant difference in the overall response due to the pulse shape effects. However, no explicit solutions exist on the mathematical treatment of the nonlinear elastic plate or effective correlation parameters such as to unify the pulse shape-dependent response curves virtually into a single one. Furthermore, evaluation of the blast nature requires investigations on pressure impulse diagrams which is beyond the scope of this study. Nevertheless, similar discrepancies exist when a comparison is made between vibration frequencies of plates examined experimentally and the FSI-FE models [53], with the measured actual frequency of vibration using the digital image correlation (DIC) being lower than the predicted FE one. Discrepancies in the experimental, analytical and numerical techniques, however, are partly inherent in the modelling techniques [70].

Second, it should be recognised that the estimated values of pressure in Table 2 are estimates based on the empirical results of Kingery-Bulmash and based on the spherical TNT detonations, a plethora of values nevertheless exist on the TNT equivalence of charges. Given a certain charge mass and diameter, the axial impulse imparted to the plate is affected by the geometry of the charge, i.e., the truncated cone (TC) charge shapes yield lower impulses than the inverted truncated cone (ITC) or cylindrical charges [62]. However, even at lower impulses, the TC plates capped while the ITC of the same charge mass induced higher impulse with no capping.

Finally, the FSI effects and pressure recirculation at the boundaries can affect the results. The reduction of the transmitted impulse to the target is brought about by the increased charge radius to plate length ratio [43].

5. Concluding Remarks

This paper deals with explicit solutions for the nonlinear elastic vibration of isotropic circular plates subjected to pulse pressure loading, which was assumed as a single term of multiplicative decomposition of its temporal part and spatial part. The temporal part of the load was considered as a rectangular pulse. As for the spatial part, a uniformly distributed pressure was considered replicating a global blast scenario.

Based on the Föppl-Von Kármán theory and ignoring the viscoelastic effects, analytical and numerical Finite Element models were proposed and analyses carried out in three folds. In the first, exact analytical solutions were derived for the case of pressures imparted statically, by using the Frobenius method, as an infinite hypergeometric series with the expression of each mode written recursively of its prior modes. The displacement field and hence the stresses are satisfied with only 6 number of terms. In the second fold, in the event of dynamically transmitted loads, by using the Variational Ritz-Galerkin method and the Lindstedt Poincaré technique, the form of PDEs were reduced to a set of coupled ODEs and solved numerically in the two phases of motion corresponding to forced and free vibrations. For an SDOF system, explicit solutions were derived.

The third fold entailed numerical 3-dimensional FE models to simulate pulse pressure loading of distal blasts in three parts. In the first, the influence of the element type on the convergence was examined using the pure Lagrangian method, the convergence was satisfied for the shell elements with an element length/thickness ratio of 1.25. Secondly, for the circumstances where the FSI effects can be ignored, parametric stuies on the influence of the plate thickness and loading magniturde were performed using the pure Lagrangian analyses and the peak captured displacement was compared in each case against that of the analytical model. The final part constituted a basis for the determination of the transient displacements in practical applications involving the FSI phenomena, but for the impulsive type loadings, in which case, a number of coupled and uncoupled MMALE models were examined representing distal blasts generated from PE4 with various charge masses. The distribution of pressure and impulse across the plate were examined.

A comparison of the analytical SDOF and MDOF models with the numerical ones revealed strong corroboration between the two, with a good degree of precision in peak transverse displacements when considering the MDOF system with three degrees of freedom. It was observed that the amplitudes of residual vibrations are less strongly correlated. It was found that while the higher modes contribute to residual vibrations, their influence is insignificant in the estimation of the maximum transverse displacements. It should also be appreciated that the frequencies of vibration obtained through FE methods and analytical formulations, although discordant at points, are in satisfactory synchrony. However, the vibration frequencies of various numerical modelling techniques are inherently distinguishable from those caprured by the DIC experimental ones.

As a final remark, the assumptions made in this study on certain aspects of the model or loading such as disregarding the influence of the pulse shape or the negative phase of the blast load limit the dynamic study to the circumstances of moderate deformations, impulsive loads and moderate scaled distances. However, the mathematical treatment of blasts with negative phase and various pulse shapes may be examined using simplified models previously proposed [8, 9, 37], or using approximate numerical analyses. This is due to the fact that deriving explicit closed-form solutions for the nonlinear elastic response of plates subject to exponential pulses, whereupon the influence of the FSI for dynamic load types may be examined, is extremely cumbersome.

6. Credit Author Statement

N. Mehreganian: Derivation, Methodology, Investigation M. Toolabi: Solution, Data analysis, Writing up Y. A. Zhuk: Methodology, Original draft preparation F. Etminan Moghadam: Visualisation, Software, Validation L.A. Louca: Supervision, Original draft preparation A. S. Fallah: Conceptualization, Methodology, Supervision, Writing up, Reviewing and Editing

Declaration of Competing Interest

The authors declare that they have no known competing financial interests or personal relationships that could have appeared to

influence the work reported in this paper.

Appendix A

A.1. The components $\beta_1 - \beta_3$ are written as

$$\beta_1 = -\frac{3p^2l^8(1-\nu^2)^2}{4096}, \beta_2 = \frac{p^2l^8(1-\nu^2)^2}{256}, \beta_3 = -\frac{9}{1024}p^2l^8(1-\nu^2)^2, \tag{A. 1 a-c}$$

The first three modes $A_2 - A_4$ of the static transverse displacement field are

$$A_2 = \frac{P_0 - 2D_1a_0A_0}{16D_1}A_4 = \left(\frac{a_0^2}{192} - \frac{b_0}{24}\right)A_0 - \frac{P_0a_0}{384D_1}A_6 = -\frac{A_0\left(a_0^3 - 32a_0b_0 - 192b_0\right)}{9216} - \frac{\left(P_0\left(-a_0^2 + 24b_0\right)\right)}{18432D_1} \tag{A. 2 a-c}$$

Substituting Eq. (37) for A_0 in (A. 2a) and then in (A. 2b-c) or using Eq. (35), the value of each mode is derived independently. While the coefficients of the function $f(\bar{r})$ are expressible as

$$a_0 = -\frac{12(1-\nu^2)}{R^2}C_2, b_0 = \frac{EhP_0^2R^4}{4096D_1^3}, \tag{A. 3a-b}$$

A2. Dynamic response

In a similar spirit to the case of static loading, the components of the stress potential function may be derived by using the Frobenius series. We assume a hypergeometric series for stress potential multiplicative of the spatial and temporal parts as:

$$\phi(t,r) = \sum_{k=0}^{\infty}\widehat{\phi}_k(t)r^{k+q} \tag{A. 4}$$

Substituting Eq. (A. 4) together with Eqs. (12a, d) into Eq. (13) with some algebraic manipulation, the left-hand side of Eq. (13) yields $-2/E[(k+q)^2(k+q-2)\widehat{\phi_k}(t)r^{k+q-2}]$ while the right-hand side is furnished to $\sum_{j=0}^{(2n)}\sum_{i=0}^{(2n)}A_iA_jr^{i+j+2}$. Since both indices i, j assume even numbers, it transpires that the index power of the stress potential function is even, leading to $q = 4$ from the indicial polynomial and k taking even numbers. The stress potential function is therefore recovered as in the expressions (41) and (42).

The components of the nonlinear function arising from the influence of membrane stresses read:

$$G_0(t) = ER^8\left[\begin{array}{c} R^4\left(\frac{3}{224}R^{14} + \frac{2}{3}a_1\right) \\ A_6(t)^3 + \left(\frac{1}{3}f_1 + \frac{1}{252}R^6\right)A_2(t)^3 + R_1^2\left(\frac{8}{15}d_1 + \frac{5}{576}R^{10}\right)A_4(t)^3 \\ +\left(\left(\frac{2}{3}R_1^4c_1 + \frac{3}{112}R_1^{14} + \frac{1}{3}a_1\right)A_2(t) + R_1^2\left(\frac{211}{6048}R_1^{14} + \frac{8}{15}a_1 + \frac{2}{3}R_1^2b_1\right)A_4(t)\right)A_6(t)^2 \\ +\left(\begin{array}{c} R_1^2\left(\frac{2}{3}R_1^2d_1 + \frac{365}{12096}R_1^{12} + \frac{8}{15}b_1\right)A_4(t)^2 + \left(\frac{2}{3}R_1^4e_1 + \frac{1}{3}b_1 + \frac{8}{15}R_1^2c_1 + \frac{277}{6048}R_1^{12}\right) \\ A_2(t)A_4(t) + \left(\frac{2}{3}R_1^4f_1 + \frac{1}{3}c_1 + \frac{109}{6048}R_1^{10}\right)A_2(t)^2 \end{array}\right) \\ A_6(t) + \left(\frac{1}{3}d_1 + \frac{79}{4032}R_1^{10} + \frac{8}{15}R_1^2e_1\right)A_2(t)A_4(t)^2 + \left(\frac{8}{15}R_1^2f_1 + \frac{1}{3}e_1 + \frac{41}{2688}R_1^8\right)A_2(t)^2A_4(t) \end{array}\right], \tag{A. 5}$$

, (A. 6)

$$G_4(t)=ER_1^{12}\Bigg[R_1^4\left(\frac{3}{5}a_1+\frac{1}{72}R_1^{14}\right)A_6(t)^3+R_1^2\left(\frac{1}{120}R_1^{10}+\frac{16}{35}d_1\right)A_4(t)^3+\left(\frac{4}{15}f_1+\frac{43}{12096}R_1^6\right)A_2(t)^3+\Bigg(\left(\frac{67}{2520}R_1^{14}+3\Big/5R_1^4c_1+4\Big/15a_1\right)A_2(t)$$

$$+R_1^2\left(\frac{7}{198}R_1^{14}+\frac{3}{5}R_1^2b_1+\frac{16}{35}a_1\right)A_4(t)\Bigg)A_6(t)^2+\left(\begin{array}{l}\left(\frac{3791}{221760}R_1^{10}+\frac{3}{5}R_1^4f_1+\frac{4}{15}c_1\right)A_2(t)^2+\left(\frac{3}{5}R_1^4e_1+\frac{16}{35}R_1^2c_1+\frac{4}{15}b_1+\frac{611}{13860}R_1^{12}\right)\\ A_4(t)A_2(t)+\left(\frac{3}{5}R_1^4d1+\frac{16}{35}R_1^2b1+\frac{59}{1980}R_1^{14}\right)A_4(t)^2\end{array}\right)A_6(t)$$

$$+\left(\frac{281}{20160}R_1^8+\frac{16}{35}R_1^2f_1+4\Big/15e_1\right)A_4(t)A_2(t)^2+\left(\frac{16}{35}R_1^2e_1+\frac{4}{15}d_1+\frac{23}{1260}R_1^{10}\right)A_4(t)^2A_2(t)\Bigg] \tag{A.7}$$

where the coefficients a_1-f_1 are

$$a_1=\frac{9R^{14}(80-13R(\nu+1))}{4480((\nu+1)R-4)},b1=\frac{(245-41R(\nu+1))R^{12}}{840((\nu+1)R-4)},c_1=\frac{(108-19(\nu+1)R)R^{10}}{480((\nu+1)R-4)},d_1=\frac{(64-11(\nu+1)R)R^{10}}{480((\nu+1)R-4)}e_1$$
$$=\frac{(50-9R(\nu+1))R^8}{240((\nu+1)R-4)},f_1=\frac{(16-3R(\nu+1))R^6}{192((\nu+1)R-4)}, \tag{A. 8a-f}$$

References

[1] B. Zakrisson, B. Wikman, H.K. Häggblad, Numerical simulations of blast loads and structural deformation from near-field explosions in air, Int. J. Impact Eng. 38 (7) (2011) 597–612, https://doi.org/10.1016/j.ijimpeng.2011.02.005.

[2] B. Zakrisson, H.-A. Haggblad, P. Jonsen, Modelling and simulation of explosions in soil interacting with deformable structures,", Cent. Eur. J. Eng. 2 (4) (2012) 532–550, https://doi.org/10.2478/s13531-012-0021-5.

[3] S.E. Rigby, et al., Measuring spatial pressure distribution from explosives buried in dry Leighton Buzzard sand, Int. J. Impact Eng. 96 (2016) 89–104, https://doi.org/10.1016/j.ijimpeng.2016.05.004.

[4] B. Fuller, et al., Effect of spatial variation of blast loading on response of plates, in: First Int. Conf. Struct. Saf. under Fire Blast (CONFAB 2015), 2015. September.

[5] S.E. Rigby, et al., Observations from preliminary experiments on spatial and temporal pressure measurements from Near-Field free air explosions, Int. J. Prot. Struct. 6 (2) (2015) 175–189, https://doi.org/10.1260/2041-4196.6.2.175.

[6] T. Børvik, A.G. Hanssen, M. Langseth, L. Olovsson, Response of structures to planar blast loads - a finite element engineering approach, Comput. Struct. 87 (9–10) (2009) 507–520, https://doi.org/10.1016/j.compstruc.2009.02.005.

[7] V. Aune, E. Fagerholt, K.O. Hauge, M. Langseth, T. Børvik, Experimental study on the response of thin aluminium and steel plates subjected to airblast loading, Int. J. Impact Eng. 90 (2016) 106–121, https://doi.org/10.1016/j.ijimpeng.2015.11.017.

[8] V. Aune, G. Valsamos, F. Casadei, M. Larcher, M. Langseth, T. Børvik, Numerical study on the structural response of blast-loaded thin aluminium and steel plates, Int. J. Impact Eng. 99 (2017) 131–144, https://doi.org/10.1016/j.ijimpeng.2016.08.010.

[9] S.E. Rigby, A. Tyas, T. Bennett, S.D. Clarke, S.D. Fay, The negative phase of the blast load, Int. J. Prot. Struct. 5 (1) (2014) 1–19, https://doi.org/10.1260/2041-4196.5.1.1.

[10] N.E. Wierschem, et al., Response attenuation in a large-scale structure subjected to blast excitation utilizing a system of essentially nonlinear vibration absorbers, J. Sound Vib. 389 (2017) 52–72, https://doi.org/10.1016/j.jsv.2016.11.003. November.

[11] P.S. Symonds, W.T. Fleming, Parkes revisited: On rigid-plastic and elastic-plastic dynamic structural analysis, Int. J. Impact Eng. 2 (1) (1984) 1–36, https://doi.org/10.1016/0734-743X(84)90013-7.

[12] E. Onat and R. Haythornthwaite, "The load carrying capacity of circular plates at large deflection," 1954, [Online]. Available: http://oai.dtic.mil/oai/oai?verb=getRecord&metadataPrefix=html&identifier=ADA951007.

[13] A. Gurkok, H.. Hopkins, The effect of geometry changes on the load carrying capacity of beams under transverse load, SIAM J. Appl. Math. 25 (3) (1973) 500–521.

[14] N. Jones, J. Gomes De Oliveira, The influence of rotatory inertia and transverse shear on the dynamic plastic behavior of beams, J. Appl. Mech. 46 (1979) 303–310, https://doi.org/10.1115/1.3424546. June 1979.

[15] N. Jones, S.-B. Kim, Q.M. Li, Response and failure of ductile circular plates struck by a mass, J. Press. Vessel Technol. 119 (3) (1997) 332, https://doi.org/10.1115/1.2842313.

[16] T WIERZBICKI, AL FLORENCE, Theoretical and experimental investigation of impulsively loaded clamped circular viscoplastic plates, Int. J. Solids Struct. 6 (5) (1970) 553–568, https://doi.org/10.1016/0020-7683(70)90030-2.

[17] N. Mehreganian, A.S Fallah, L.A. Louca, Inelastic dynamic response of square membranes subjected to localised blast loading, Int. J. Mech. Sci. 148 (2018) 578–595, https://doi.org/10.1016/j.ijmecsci.2018.09.017. August.

[18] N. Mehreganian, A.S. Fallah, L.A. Louca, Plastic dynamic response of simply supported thick square plates subject to localised blast loading, Int. J. Impact Eng. 126 (2019) 85–100, https://doi.org/10.1016/j.ijimpeng.2018.12.010. December 2018.

[19] N.S. Rudrapatna, R. Vaziri, M.D. Olson, Deformation and failure of blast-loaded square plates, Int. J. Impact Eng. 22 (4) (1999) 449–467, https://doi.org/10.1016/S0734-743X(98)00046-3.

[20] P. Patr and W. Krauth, "Numerical solutions of the von karman equations for a thin plate," pp. 1–8, 1996.

[21] P.A.A. Hooper, R.A.M.A.M. Sukhram, B.R.K.R.K. Blackman, J..P. Dear, On the blast resistance of laminated glass, Int. J. Solids Struct. 49 (6) (2012) 899–918, https://doi.org/10.1016/j.ijsolstr.2011.12.008.

[22] P. Del Linz, et al., An analytical solution for pre-crack behaviour of laminated glass under blast loading, Compos. Struct. 144 (2016) 156–164, https://doi.org/10.1016/j.compstruct.2016.02.058.

[23] Y. Yuan, P.J. Tan, Y. Li, Dynamic structural response of laminated glass panels to blast loading, Compos. Struct. 182 (2017) 579–589, https://doi.org/10.1016/j.compstruct.2017.09.028. August.

[24] E. Borenstein, H. Benaroya, Sensitivity analysis of blast loading parameters and their trends as uncertainty increases, J. Sound Vib. 321 (3–5) (2009) 762–785, https://doi.org/10.1016/j.jsv.2008.10.017.

[25] E.H. Dowell, C.S. Ventres, Comparison of theory and experiment for nonlinear flutter of loaded plates, AIAA J 8 (11) (1970) 2022–2030, https://doi.org/10.2514/3.6041.

[26] W. Zhang, T. Liu, A. Xi, Y.N. Wang, Resonant responses and chaotic dynamics of composite laminated circular cylindrical shell with membranes, J. Sound Vib. 423 (2018) 65–99, https://doi.org/10.1016/j.jsv.2018.02.049. March.

[27] W. Zhang, J. Yang, Y. Hao, Chaotic vibrations of an orthotropic FGM rectangular plate based on third-order shear deformation theory, Nonlinear Dyn 59 (4) (2010) 619–660, https://doi.org/10.1007/s11071-009-9568-y.

[28] M.L. Dano, M.W. Hyer, Thermally-induced deformation behavior of unsymmetric laminates, Int. J. Solids Struct. 35 (17) (1998) 2101–2120, https://doi.org/10.1016/S0020-7683(97)00167-4.

[29] S. Vidoli, Discrete approximations of the Föppl – Von Kármán shell model : From coarse to more refined models, Int. J. Solids Struct. 50 (9) (2013) 1241–1252, https://doi.org/10.1016/j.ijsolstr.2012.12.017.

[30] Z. Kazanci, Z. Mecitoğlu, Nonlinear dynamic behavior of simply supported laminated composite plates subjected to blast load, J. Sound Vib. 317 (3–5) (2008) 883–897, https://doi.org/10.1016/j.jsv.2008.03.033.

[31] S. Daynes, K.D. Potter, P.M. Weaver, Bistable prestressed buckled laminates, Compos. Sci. Technol. 68 (15–16) (2008) 3431–3437, https://doi.org/10.1016/j.compscitech.2008.09.036.

[32] E.. Mansfield, bending, buckling and curling of a heated elliptical plate, Proc. R. Soc. A Math. Phys. Eng. Sci. 268 (1334) (1965) 316–327.

[33] T. Liu, W. Zhang, J.. Wang, Nonlinear dynamics of composite laminated circular cylindrical shell clamped along a generatrix and with membranes at both ends, Nonlinear Dyn 90 (2) (2017) 1393–1417, https://doi.org/10.1007/s11071-017-3734-4.

[34] S.A. Emam, A Theoretical and Experimental Study of Nonlinear Dynamics of Buckled Beams, PhD Thesis, Virginia Polytechnic Institute and State University, 2002.

[35] A.H. Nayfeh, S.A. Emam, Exact solution and stability of postbuckling configurations of beams, Nonlinear Dyn 54 (4) (2008) 395–408, https://doi.org/10.1007/s11071-008-9338-2.

[36] A.H. Nayfeh, Introduction to Perturbation Techniques, 20, Wiley-Interscience Publication, New York, 1993.

[37] N. Mehreganian, A.S.S. Fallah, L.A.A. Louca, Nonlinear dynamics of locally pulse loaded square Föppl–von Kármán thin plates, Int. J. Mech. Sci. 163 (2019), https://doi.org/10.1016/j.ijmecsci.2019.105157. February.

[38] W. Zhang, Global and chaotic dynamics for a parametrically excited thin plate, J. Sound Vib. 239 (5) (2001) 1013–1036, https://doi.org/10.1006/jsvi.2000.3182.

[39] T.-L. Teng, C.-C. Liang, Transient dynamic large-deflection analysis of panel structure under blast loading, Japan Soc. Mech. Eng. 339 (4) (1996) 591–597, https://doi.org/10.1248/cpb.37.3229.

[40] G.I. Taylor, The pressure and Impulse of Submarine Explosion Waves on Plates, in: G.K. Batchelor, C.F. Sharman, J.W. Maccoll, R.M. Davies, H. Jones, P. G. Saffman (Eds.), The Scientific Papers of Sir Geoffrey Ingram Taylor: Vol 3 Aerodynamics and the Mechanics of Projectiles and Explosions, vol. III, no. 4, Eds, Cambridge University Press, Cambridge, UK, 2011, p. 590.

[41] N. Kambouchev, R. Radovitzky, L. Noels, Fluid–structure interaction effects in the dynamic response of free-standing plates to uniform shock loading, J. Appl. Mech. 74 (5) (2007) 1042, https://doi.org/10.1115/1.2712230.

[42] N. Kambouchev, L. Noels, R. Radovitzky, Nonlinear compressibility effects in fluid-structure interaction and their implications on the air-blast loading of structures, J. Appl. Phys. 100 (6) (2006) 1–11, https://doi.org/10.1063/1.2349483, 063519.

[43] D. Bonorchis, G.N. Nurick, The influence of boundary conditions on the loading of rectangular plates subjected to localised blast loading - Importance in numerical simulations, Int. J. Impact Eng. 36 (1) (2009) 40–52, https://doi.org/10.1016/j.ijimpeng.2008.03.003.

[44] Q.M. Li, H. Meng, Pressure-impulse diagram for blast loads based on dimensional analysis and single-degree-of-freedom model, J. Eng. Mech. 128 (1) (2002) 87–92. Doi 10.1061/(Asce)0733-9399(2002)128:1(87).

[45] A.S. Fallah, L.A. Louca, Pressure-impulse diagrams for elastic-plastic-hardening and softening single-degree-of-freedom models subjected to blast loading, Int. J. Impact Eng. 34 (4) (2007) 823–842, https://doi.org/10.1016/j.ijimpeng.2006.01.007.

[46] A. Kumar, S.K. Saha, V.A. Matsagar, Stochastic response analysis of elastic and inelastic systems with uncertain parameters under random impulse loading, J. Sound Vib. 461 (2019), 114899, https://doi.org/10.1016/j.jsv.2019.114899.

[47] R. Szilard, Theories and Applications of Plate Analysis : Classical Numerical and Engineering Methods, Wiley-Interscience Publication, New York, 2004.

[48] S. Timoshenko, S. Woinosky-Kreiger, Theory of Plates and Shells, McGraw Hill Book Company, Inc., Second. New York, 1959.

[49] A. D. Polyanin and V. F. Zaitsev, Handbook of Exact Solutions for Ordinary Differential Equations, 2nd ed. London: Chapman and Hall, 2002.

[50] E. Kreyszig, Advanced Engineering Mathematics, 10th ed., no. 181. Hoboken, NJ ; Chichester: John Wiley & Sons, 2011.

[51] A. Wang, H. Chen, W. Zhang, Nonlinear transient response of doubly curved shallow shells reinforced with graphene nanoplatelets subjected to blast loads considering thermal effects, Compos. Struct. 225 (2019), 111063, https://doi.org/10.1016/j.compstruct.2019.111063. May.

[52] T. Liu, W. Zhang, J.J. Mao, Y. Zheng, Nonlinear breathing vibrations of eccentric rotating composite laminated circular cylindrical shell subjected to temperature, rotating speed and external excitations, Mech. Syst. Signal Process. 127 (2019) 463–498, https://doi.org/10.1016/j.ymssp.2019.02.061. July.

[53] N. Mehreganian, L.A. Louca, G.S. Langdon, R.J. Curry, N. Abdul-Karim, The response of mild steel and armour steel plates to localised air-blast loading-comparison of numerical modelling techniques, Int. J. Impact Eng. 115 (2018) 81–93, https://doi.org/10.1016/j.ijimpeng.2018.01.010. January.

[54] D. Bonorchis, G.N. Nurick, The effect of welded boundaries on the response of rectangular hot-rolled mild steel plates subjected to localised blast loading, Int. J. Impact Eng. 34 (11) (2007) 1729–1738, https://doi.org/10.1016/j.ijimpeng.2006.11.002.

[55] M. Toolabi, A.S. Fallah, P.M. Baiz, L.A. Louca, Dynamic analysis of a viscoelastic orthotropic cracked body using the extended finite element method, Eng. Fract. Mech. 109 (2013) 17–32, https://doi.org/10.1016/j.engfracmech.2013.06.003.

[56] M. Toolabi, A.S. Fallah, P.. Baiz, L.. Louca, Enhanced mixed interpolation XFEM formulations for discontinuous Timoshenko beam and Mindlin-Reissner plate, Int. J. Numer. Methods Eng. 115 (2018) 1–24, https://doi.org/10.1002/nme.5822. August.

[57] Y. Yang, A.S. Fallah, L.A. Louca, Frequency analysis of a heterogeneous perforated panel using a super-element formulation, J. Sound Vib. 327 (1–2) (2009) 26–40, https://doi.org/10.1016/j.jsv.2009.05.017.

[58] Dassault Systèmes Simulia, "Abaqus 6.1 2 (Analysis User's Manual)," vol. V. 2012.

[59] N. Mehreganian, A.S.S. Fallah, G.K.K. Boiger, L.A.A. Louca, Response of armour steel square plates to localised air blast load- a dimensional analysis, Int. J. Multiphys. 11 (4) (2017) 1–20, https://doi.org/10.21152/1750-9548.11.4.387.

[60] K. Micallef, et al., On dimensionless loading parameters for close-in blasts, Int. J. Multiphys. 9 (2) (2015) 193 [Online]Available, http://scholar.google.com/scholar?hl=en&btnG=Search&q=intitle:On+dimensionless+loading+parameters+for+close-in+blasts#0.

[61] UFC 3-340-02, Structures to resist the effects of accidental explosions, Struct. Congr. 2011 (2008) 1867, https://doi.org/10.1061/41171(401)127. May 2005.

[62] G.N. Nurick, S. Mahoi, G.S. Langdon, The response of plates subjected to loading arising from the detonation of different shapes of plastic explosive, Int. J. Impact Eng. 89 (2016) 102–113, https://doi.org/10.1016/j.ijimpeng.2015.11.012. November.

[63] K. Micallef, A.S. Fallah, P.T. Curtis, L.A. Louca, On the dynamic plastic response of steel membranes subjected to localised blast loading, Int. J. Impact Eng. 89 (2016) 25–37, https://doi.org/10.1016/j.ijimpeng.2015.11.002.

[64] K. Micallef, B. Eng, A. H. Melit, and M. Sc, "The dynamic response of blast-loaded monolithic and composite plated structures A thesis submitted for the degree of Doctor of Philosophy (Ph . D .).".
[65] K. Micallef, A.S. Fallah, D.J. Pope, L.A. Louca, The dynamic performance of simply-supported rigid-plastic circular steel plates subjected to localised blast loading, Int. J. Mech. Sci. 65 (1) (2012) 177–191, https://doi.org/10.1016/j.ijmecsci.2012.10.001.
[66] P. S. Symonds and T. Wierzbicki, "Membrane mode solutions for impulsively loaded circular plates," vol. 46, no. March 1979, pp. 58–64, 2015.
[67] N. Jones, Dynamic inelastic response of strain rate sensitive ductile plates due to large impact, dynamic pressure and explosive loadings, Int. J. Impact Eng. 74 (2014) 3–15, https://doi.org/10.1016/j.ijimpeng.2013.05.003.
[68] P.S. Symonds, Finite elastic and plastic deformations of pulse loaded structures by an extended mode technique, Int. J. Mech. Sci. 22 (10) (1980) 597–605, https://doi.org/10.1016/0020-7403(80)90076-4.
[69] N. Mehreganian, A. Soleiman Fallah, L.A. Louca, Large elastic-plastic deformation of square membranes subjected to localised pulse pressure loads, Bull. Taras Shevchenko Natl. Univ. Kyiv. Ser. Phys. Math. 1 (Jan. 2019) 126–133, https://doi.org/10.17721/1812-5409.2019/1.29.
[70] P.S. Symonds, T.X. Yu, Counterintuitive behaviour in a problem of elastic-plastic beam dynamics, J. Appl. Mech. 52 (85) (1985) 517–522.